

In-situ observations of strong waves in ice amplitude modulation with a 12-hour period: a likely signature of complex physics governing waves in ice attenuation?

J. Rabault^{1,*}, T. Halsne^{2,3}, A. Carrasco¹, A. Korosov⁴, J. Voermans⁵, P. Bohlinger², J.B. Debernard¹, M. Müller^{1,9}, Ø. Breivik^{2,3}, T. Nose⁶, G. Hope², F. Collard⁷, S. Herlédan⁷, T. Kodaira⁶, N. Hughes⁸, Q. Zhang⁸, K.H. Christensen^{1,9}, A. Babanin⁵, L. W. Dreyer⁹, C. Palerme¹, L. Aouf¹⁰, K. Christakos², A. Jensen⁹, J. Röhrs¹, A. Marchenko¹¹, G. Sutherland¹², T.K. Løken¹³, and T. Waseda⁶

¹Norwegian Meteorological Institute, Oslo, Norway

²Norwegian Meteorological Institute, Bergen, Norway

³The University of Bergen, Bergen, Norway

⁴Nansen Environmental and Remote Sensing Center, Bergen, Norway

⁵The University of Melbourne, Melbourne, Australia

⁶The University of Tokyo, Kashiwa, Japan

⁷OceanDataLab, Locmaria-Plouzane, France

⁸Norwegian Meteorological Institute, Tromsø, Norway

⁹The University of Oslo, Oslo, Norway

¹⁰Météo France, CNRM-CNRS, UMR-3589, Toulouse, France

¹¹The University Center in Svalbard, Longyearbyen, Norway

¹²Environment Climate Change Canada, Dorval, Canada

¹³Nord University, Bodø, Norway

*corresponding author: Jean Rabault (jean.rblt@gmail.com)

ABSTRACT

The Marginal Ice Zone (MIZ) forms a critical transition region between the ocean and sea ice cover as it protects the close ice further in from the effect of the steepest and most energetic open ocean waves. As waves propagate through the MIZ, they get exponentially attenuated. Unfortunately, the associated attenuation coefficient is difficult to accurately estimate and model, and there are still large uncertainties around which attenuation mechanisms dominate depending on the conditions. This makes it challenging to predict waves in ice attenuation, as well as the effective impact of open ocean waves propagating into the MIZ on sea ice breakup and dynamics. Here, we report in-situ observations of strongly modulated waves-in-ice amplitude, with a modulation period of around 12 hours. We show that simple explanations, such as changes in the incoming open water waves, or the effect of tides and currents and bathymetry, cannot explain for the observed modulation. Therefore, the significant wave height modulation observed in the ice most likely comes from a modulation of the waves-in-ice attenuation coefficient. To explain this, we conjecture that one or several waves-in-ice attenuation mechanisms are periodically modulated and switched on and off in the area of interest. We gather evidence that sea ice convergence and divergence may be the factor driving this change in the waves in ice attenuation mechanisms and attenuation coefficient, for example by modulating the intensity of floe-floe interaction mechanisms. Since this conclusion is obtained, at least partially, by elimination, we acknowledge that additional measurements will be needed to provide a positive proof of our conjecture. We suggest that additional data could be gathered in future field experiments, by performing additional measurements in the area in both open water and ice infested conditions, and by programming waves in ice buoys to transmit additional statistics describing the occurrence and strength of floe collisions and the response amplitude operator of the ice floes they are deployed on. This would allow to detect, identify, and count, floe-floe collisions and the intensity of floe-floe interaction mechanisms in future waves in ice measurement campaigns.

1 Introduction

Sea ice is an important component in the global climate and weather system: in their respective late winters, Arctic sea ice covers typically around 15.5 million square kilometers, and Antarctic sea ice around 18.5 million square kilometers (averages are computed for the reference period 1981-2010, and the Arctic sea ice September extent trend is decreasing by about 12 percent per decade)^{1,2}. Averaged over the year, sea ice covers around 25 millions square kilometers (though the trend is decreasing), corresponding to around 7% of the area of the global oceans³. Sea ice has, therefore, a major effect on the energy fluxes and physical oceanography of the polar regions, and a large impact on Earth's weather and climate dynamics as a whole⁴⁻⁶. Moreover, sea ice sets drastic constraints on human activities, in particular in the Arctic where shipping, fishing, logistics, and industrial activities are increasing⁷⁻⁹.

A particularly important region of the sea ice is the Marginal Ice Zone (MIZ). The MIZ is the area of the sea ice that is heavily influenced by phenomena happening in the open ocean, in particular, surface waves. The interaction and two-way coupling between the MIZ and the incoming surface waves and swells has a large impact on several key sea ice mechanisms, such as sea ice breakup, melting, and drift^{10,11}. This coupling can have large scale effects on the extent and evolution of the sea ice, especially as a number of two-way coupling mechanisms exist¹²⁻¹⁴. For example, sea ice breakup and melting is currently leading to the appearance of new open water areas in the Arctic, which in turn provides more fetch for waves to grow, and to break even more sea ice¹⁵. Similarly, albedo and solar radiation absorption mechanisms lead to self-reinforcing dynamics: since sea ice reflects up to 85% of incoming solar radiation, while the ocean absorbs up to around 90% of solar radiation, sea ice melting leads to a self-reinforcing solar radiation energy absorption and temperature increase¹⁶.

The two-way coupling between waves and ice in the MIZ is related to a number of physical phenomena, in particular:

- Wave attenuation¹⁷⁻²²: as waves propagate in the MIZ, these get progressively attenuated by a number of mechanisms. While it is not completely clear at present which mechanisms dominate in which conditions, most attenuation mechanisms result, in theory, in an amount of energy dissipation that is proportional to the local wave energy, hence an exponential wave damping as a function of propagation distance. More specifically, the underlying physics can be associated to a combination of viscous damping at the water-ice interface^{18,23-25}, turbulence²⁶, viscoelasticity²⁷⁻²⁹, diffraction³⁰, scattering³¹, collisions and floe-floe interactions^{32,32,33}.
- Sea ice breakup^{27,34,35}: waves with sufficient amplitude, and applied for long enough, can break the sea ice following a number of flexion and fatigue mechanisms^{34,36}.
- Sea ice drift and melting³⁷: once the waves have broken the sea ice, sea ice can drift more freely, leading to different drift properties. In addition, wave attenuation combined with wave momentum conservation results in a wave radiation stress, which can also be a mechanism driving sea ice drift in the MIZ and ice edge displacements³⁸.
- Fetch modification effects resulting from the presence or absence of sea ice¹⁵: sea ice, by modulating the ocean-atmosphere coupling, affects how much effective fetch is available to cause the growth of waves in ice-infested waters.

The combination of these effects makes for complex dynamics happening in the MIZ. This is made even more challenging by the intrinsic complexity of sea ice as a material: depending on temperature, salinity, and the history of the mechanical stress and temperature experienced by sea ice, its mechanical properties can vary by up to 1 order of magnitude, with significant changes possibly taking place even within a timescale of a few days³⁹⁻⁴¹. Moreover, a number of additional variables, such as the floe size distribution (FSD)⁴²⁻⁴⁵, are making the whole picture even more complex, as e.g. FSD can change quickly through the effect of wind and waves⁴², and modulate all aspects of sea ice dynamics.

In addition to the intrinsically complex physics involved in sea ice dynamics and the MIZ, sea ice and waves-in-ice in-situ data are relatively scarce. While several expeditions are taking place in the sea ice every year, instrumentation deployments have traditionally been limited due to the intrinsic cost of waves-in-ice buoys. Recently, a new trend has emerged, which consists in deploying large numbers of waves in ice buoys, leveraging open source technologies to reduce the cost of individual buoys by around an order of magnitude compared to the commercial instrumentation that has been available traditionally⁴⁶⁻⁴⁸. This approach, which has been pioneered, among others, by the OpenMetBuoys (OMBs) series of instruments^{46,47,49} (developed by our group), and other similar instruments (e.g., the MicroSWIFT,⁵⁰), is now starting to provide larger and more representative amounts of data about the MIZ. This, combined with open data release policies, is starting to enable new in-situ based studies of the MIZ, focused on the use of hi-density, hi-accuracy waves in ice measurements⁵¹⁻⁵³. Such a trend is now making it possible to improve the validation of models⁵², and will also, possibly, allow much needed further development of geophysical transfer function for interpreting satellite images⁵⁴⁻⁵⁷, as well as improving process understanding. As a consequence, a number of campaigns are now deploying OMBs en masse, allowing to generate significant amounts of data about regions which have traditionally been undersampled, and providing new inputs to sea ice scientists and modelers.

In the present paper, we focus on in-situ data retrieved from an OMB deployment which took place in 2021, and that presents complex patterns of waves in ice significant wave height (SWH) modulation. We show that the evolution in the SWH very likely cannot be explained by neither classical mechanisms such as wave-current interaction, nor by present wave models including state-of-the-art waves in ice damping parameterization. Therefore, we conjecture that this observation that cannot be reproduced in state-of-the-art numerical models is likely the signature that some physics are currently missing in these models.

The structure of the manuscript is as follows. We first present the different sources of data and numerical models available to perform our case study. We then proceed on analysing the results of the models and in-situ data, investigating if these are able to reproduce the in-situ observations. Finally, we discuss possible explanations for the observed dynamics, and we both formulate a conjecture around the nature of candidate mechanisms that could produce the features observed, as well as suggest how this conjecture could be tested in further measurement campaigns.

2 Data sources

In this section, we present the different sources of data used in the analysis and discussion, and show their main features.

2.1 Observation data sources

2.1.1 Buoy data: direct observations of drift and 1-dimensional wave spectra

The core of the observations presented here is a series of waves in ice buoys trajectories and wave observations collected between February and March 2021 in the Barents Sea, South East of Svalbard, using OMBs v2018⁴⁶ and v2021⁴⁷ (the v2021 deployed were prototypes, and not all OMBs v2021 were equipped with wave measurement hardware). These data are already openly released and presented in detail in⁵¹, and we refer the reader curious of technical details to the corresponding publication and the cruise report⁵⁸. To summarize, OMBs report sea ice drift tracks (as observed from GPS measurements) and waves in ice 1-dimensional spectra (as observed from Inertial Motion Units (IMU) measurements), both transmitted in near-real-time over the iridium network.

The deployment of the OMBs used in this study took place in February 2021 in the Barents Sea East of Svalbard, with the deployment details being reported in⁵⁸. The specific wave event we focus on took place between March 1st 2021 and March 4th 2021. As visible in Fig. 1, 9 OMBs were present in the area, and covered a range of depths in the MIZ. The SWH reported by these instruments is presented in Fig. 1, and the wave spectrum for the instruments furthest into the MIZ (IDs 19648, 200905, 13319) are visible in Fig. 2. In the following, we will refer to the buoys with IDs 19648, 200905, 13319, as the "buoys of interest" (BOIs).

The dominating feature visible in Figs. 1, 2 is the strong modulation, with a period of around 12 hours, that is visible in the SWH and the 1D wave spectrum of the instruments inside the MIZ. This modulation is visible consistently across several instruments located in the MIZ, both v2018 and v2021. Instruments situated on the very edge, or outside, of the MIZ, do not display such modulated SWH patterns. This modulated SWH pattern is an outstanding feature in the present dataset, and the following analysis will be focused on understanding this specific event. While rapid increases in the SWH observed in sea ice have been observed in the past and related to, e.g., sea ice breakup induced by propagating wave trains⁵⁹, the present data are unique in that a periodic increase and decrease in the SWH is observed.

For the BOI 19648, which is the deepest in the MIZ and has the highest temporal resolution (since it is an instrument v2021), a significant wave height $SWH_{T00}=0.33\text{m}$ is observed at 2021-03-02T00:00Z, before reducing to $SWH_{T06}=0.03\text{m}$ at T06:01Z, and increasing again to $SWH_{T12}=0.34\text{m}$ at T12:00Z. This represents a modulation ratio between the maximum and minimum SWH reported within 12 hours, $(SWH_{T00} - SWH_{T06})/SWH_{T00}$, of over 90%. We note that the actual modulation ratio may be even higher than our analysis reveals, since (i) the 0.03m SWH reported at T06:01Z comes close to the noise background of the instrument, so that the SWH value reported then may include some level of noise and may be slightly higher than the actual SWH at the location of the instrument. Moreover, (ii) the time resolution of the SWH measurements for instrument 19648, though higher than for the other instruments, is still only every 2 hours, so it is likely that the "coarsely sampled" minimum (resp. maximum) measured does not match exactly the time when the actual minimum (resp. maximum) SWH is reached in reality. The typical peak wave period in the outer part of the MIZ is around 12s, and at the BOIs it is around 14s through the event, as visible in Fig. 2. These values are typical for records of waves in ice in the area.

A clear general drift pattern is visible in the GPS tracks of the buoys. All buoys drift generally to the South-South-West over the duration of the event, with additional motion taking place at a period of around 12 hours, likely due to a combination of inertial oscillation and tidal currents (both have around the same period in this area), as visible specifically for the BOIs in Fig. 3. This general sea ice drift motion is accompanied by strong shear and convergence / divergence motion in the sea ice. To illustrate this, we analyse the triangle element obtained by combining the 3 BOIs, and we compute the associated divergence by (i) interpolating the position of the buoys on a common time base, (ii) using a first order finite difference in time to compute an estimate of the velocity of the 3 BOIs on this common time base, (iii) computing the local divergence following the methodology of⁶⁰:

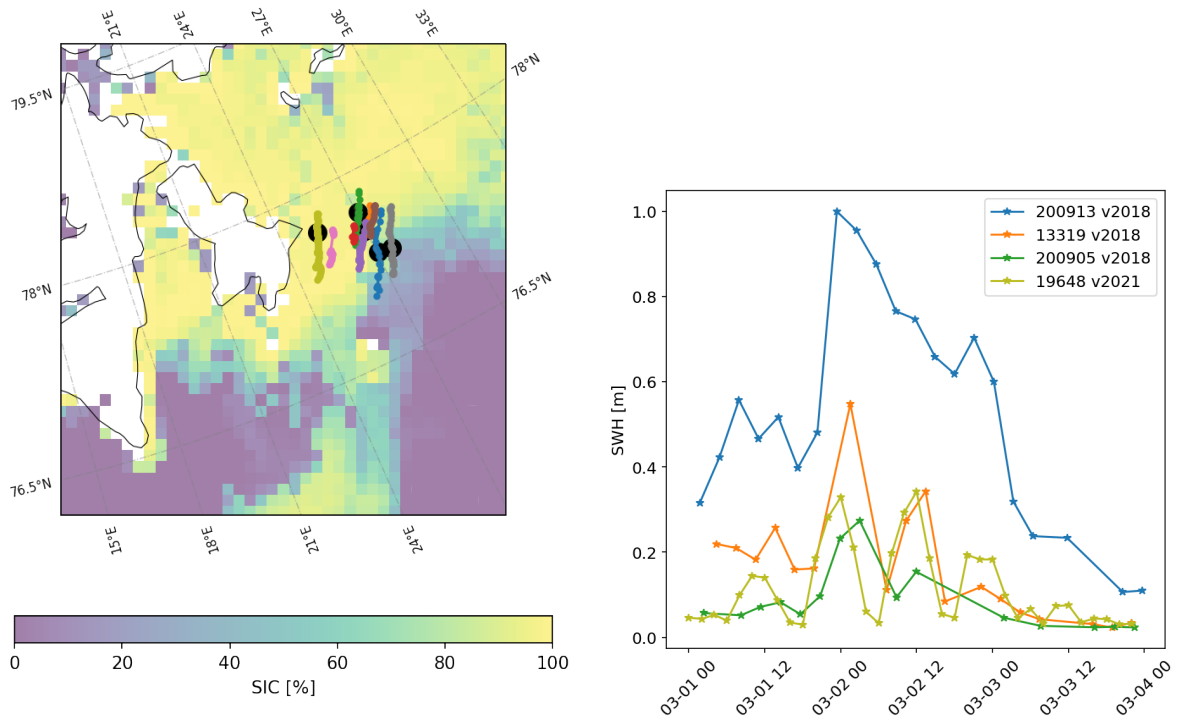


Figure 1. Overview of the buoy deployment during the modulated significant wave height event. A total of 9 buoys are clustered in the same area at the South East of Svalbard around 2021-03-01. The overview map subfigure (left) presents the sea ice concentration (SIC, data source: internal product at the Norwegian Meteorological Institute, obtained from combining AMSR2 passive microwave observations and Sentinel-1 SAR observations) at 2021-03-02T06:00Z, around the middle of the time window of the SWH modulation event. The black dots indicate the position of the buoys at the corresponding time, and the trajectory for each buoy is indicated in a separate color, corresponding to the caption on the SWH subfigure. The SWH subfigure (right) shows the timeseries of the SWH for the instruments for which these are available without excessive dropout rates. The instruments furthest into the MIZ show clear SWH modulation with a period of around 12 hours (instruments with IDs 19648, 200905, 13319 in particular, which we call "buoys of interest" (BOIs) in the following; these are the ones we focus on in the rest of this work). Note that not all prototypes of instruments v2021 are equipped with an IMU and wave measurement capability. The key feature of this dataset is the 12-hour modulation in the SWH observed by the buoys into the ice. Instrument 19648, which is the deepest into the MIZ, displays a modulation ratio between the maximum and minimum SWH it observes over 12 hours of up to 90%.

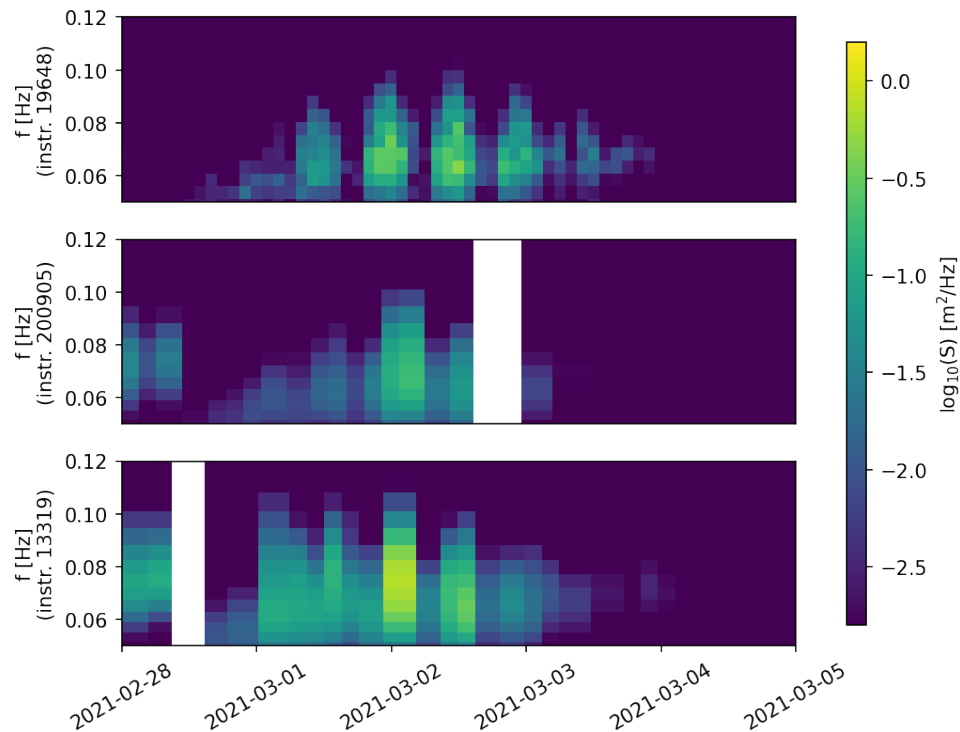


Figure 2. 1-dimensional wave spectrum for the 3 instruments furthest in the MIZ that are equipped with wave measurement capability (referred to as the Buoys Of Interest (BOIs) with IDs 19648, 200905, 13319), obtained during the time of the modulated SWH wave event. The instrument ID 19648 is a v2021 prototype, with higher wave measurement rate, a higher frequency resolution for the transmitted 1D spectra, and more sophisticated wave spectrum buffering and iridium transmission retry strategy than the 2 other v2018 instruments, resulting in better resolution of the wave spectra in both time and frequency and fewer missing measurements. The modulation in the wave activity is clearly visible on all instruments, and is particularly striking on the instrument ID 19648 thanks to its higher temporal resolution. The wave spectra shown here confirm that the SWH oscillatory event observed in Fig. 1 corresponds to an increase and decrease of the wave activity over the full frequency range, is observed consistently across instruments, and is not the result of some measurement artifacts.

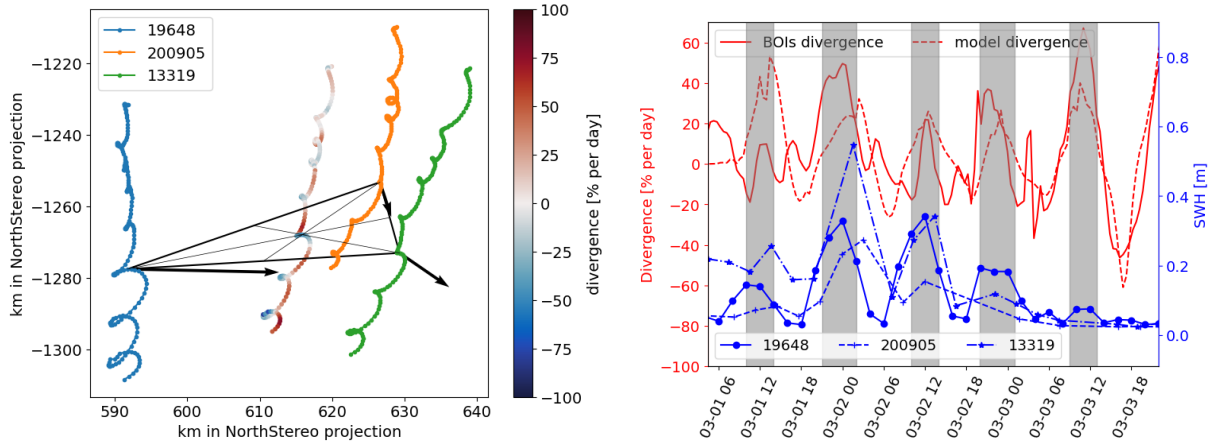


Figure 3. Details of the drift pattern observed for the 3 BOIs. Left: zoom-in onto the drift trajectories for the BOIs over the period 2021-02-29 to 2021-03-03. A clear drift pattern from North to South is observed. In addition, higher frequency motion (with a period of around 12 hours) is visible. We also show the barycenter of the 3 BOIs, which we color by the instantaneous value of the motion divergence, computed based on the triangle element formed by the 3 BOIs. The black triangle and arrows illustrate one instantaneous triangle element, its associated barycenter, and the velocity of the 3 BOIs at the corresponding time. Right: illustration of the instantaneous divergence rate computed for the BOIs triangle ("BOIs divergence" curve), alongside the SWH measured by the BOIs; a clear correlation is observed. The locally averaged sea ice divergence from the sea ice numerical model (curve "model divergence", see section 2.2.3) is also included, and shows good agreement with our in-situ measurements, which is a cross validation of the sea ice model quality.

$$\nabla \cdot \mathbf{u} = u_x + v_y, \quad (1)$$

where $\nabla \cdot \mathbf{u}$ is the sea ice velocity divergence, with $\mathbf{u} = (u, v)$ the sea ice velocity in the East-West and North-South directions, and u_x and v_y are the spatial gradients in BOIs motion computed using a line integral along the boundary of the triangle:

$$u_x = \frac{1}{A} \oint u dy, v_y = -\frac{1}{A} \oint v dx, \quad (2)$$

where A is the triangle area. The line integrals are approximated based on the motion of the BOIs at the edges of the triangle element interpolated in time on the common time base, similar to⁶⁰. For example, we compute $\oint u dy$ as:

$$\oint u dy = \sum_{i=1}^3 \frac{1}{2} (u_{i+1} + u_i) (y_{i+1} - y_i), \quad (3)$$

where the subscripts are cyclical (i.e., $u_4 = u_1$), and we have used centered finite differences for $u \approx (u_{i+1} + u_i)/2$ and $dy \approx (y_{i+1} - y_i)$, similar to⁶⁰. Following⁶⁰, this results in a trapezoidal rule for linear interpolation of u between BOIs. Similar formulas can be written down for the other partial derivatives, and the area A is computed as:

$$A = \frac{1}{2} \sum_{i=1}^3 (x_i y_{i+1} - y_i x_{i+1}). \quad (4)$$

The algorithm and code used for the computation of the divergence are available in a notebook on the GitHub data and code release page (see link in Appendix). The divergence coefficient obtained is presented in Fig. 3. Strong sea ice convergence and divergence patterns are observed, consistently with previous reports in the same area⁶¹. As visible there, a clear correlation exists between the modulation observed in the SWH, and the local divergence rate. This will be discussed in details later in the manuscript.

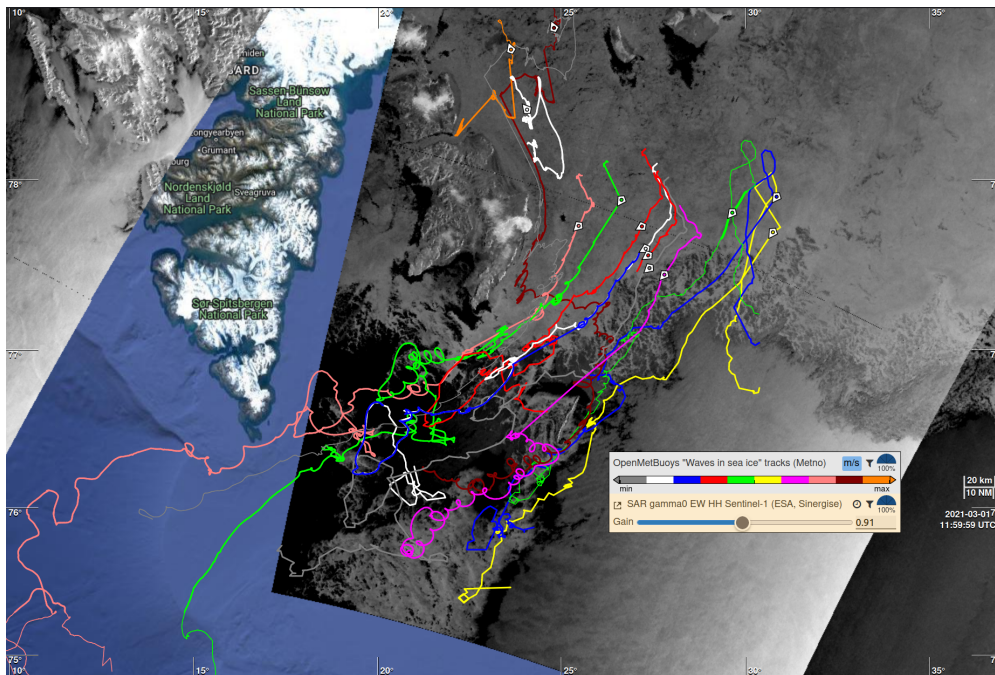


Figure 4. SAR overview of the OMB locations East of Svalbard at the reference time 2021-03-01T12Z. Sea ice is clearly visible from Sentinel-1 SAR gamma-0 EW observations (the time width for collocation matching is taken equal to 1 day). Each line indicates an OMB trajectory, and the position of each buoy at the reference time is indicated by a marker. As visible on the SAR image, the BOIs are well within the MIZ, in the middle of an area of broken ice floes. The illustration is generated using the Ocean Virtual Laboratory online viewer⁶⁴, and it can be re-generated and explored interactively using the permalink: <https://odl.bzh/RqDJgsDe> (accessed November 2023; note that minor cosmetic changes need to be applied to exactly reproduce the figure, see the notes in Appendix).

2.1.2 Sea ice imaging using SAR satellite data

We also look directly into satellite images available over the area to further visually confirm, based purely on direct satellite observations, that the sea ice conditions correspond to the models and that the instruments are well inside the MIZ during the event. An overview of the sea drifters and sea ice conditions observed directly from Synthetic Aperture Radar (SAR, gamma-0 from Sentinel-1 in EW mode⁶²) is provided in Fig. 4. As visible there, and in good agreement with the figures presented above, the BOIs are well within the MIZ over the duration of the modulated SWH event.

A closer look at Sentinel-1 SAR image acquired on 2021-03-01 (Fig. 5, left) reveals sub-mesoscale ocean eddy (10 km in diameter) near the southern end of the Hopen island, in good agreement to previous observations and numerical models results⁶³. The next Sentinel-1 SAR image acquired on a similar region (5, right) shows a similar pattern near the southern edge, and a mushroom-like structure near the northern edge. Both images confirm the presence of strong tidal or inertial oscillation currents in the region, which generate intense sea ice motion and strong patterns of sea ice convergence and divergence.

The SAR images can also be used to estimate the kind of sea ice conditions locally present in both the outer MIZ and around the BOIs. Several SAR images zoom-ins are presented in Fig. 6, both in the outer MIZ (subfigures (a) and (b)), at the location of BOI 19648 (subfigure (c)), and much further North (subfigure (d), used as a reference to illustrate conditions with large unbroken ice floes). Fig. 6 confirms that waves propagate over the ice tongue South-West from the BOIs, and that floe sizes of typically a few hundreds of meters are observed around the BOIs. Therefore, this further confirms that the sea ice around the BOIs is constituted of ice floes with dimensions typically comparable to the wavelength, and that the sea ice likely does not behave like a single continuous solid plate, similar to what is reported by e.g. by²⁰ when cracks and discontinuities are present in the ice cover. This is consistent with the observation of strong sea ice convergence and divergence patterns. Indeed, in order for the ice cover to be able to sustain large divergence and convergence, there must be enough areas of open water leads that can open and close in order to sustain the "compression", respectively "extension", of the ice cover.

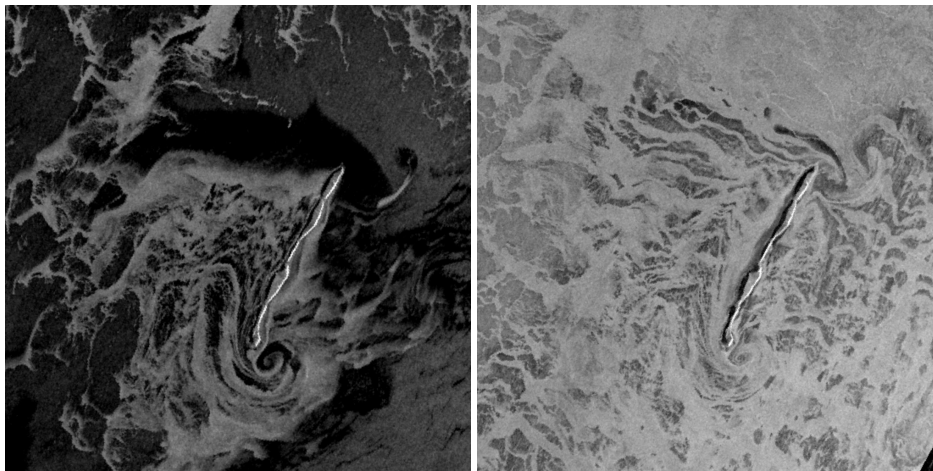


Figure 5. A close look on two Sentinel-1 SAR images, acquired on 2021-03-01T05:26:01Z (left, permalink: <https://odl.bzh/K8Gf8seu>) and on 2021-03-04T06:39:42Z (right, permalink: <https://odl.bzh/BFidlhn1>) over Hopen island. This confirms the existence of strong sea ice motions induced by tides and inertial oscillations.

2.1.3 Historic wave measurements in the area using satellite measurements over ice-free water

We use the open source tool wavy¹ to retrieve satellite measurements of the SWH when no sea ice is present in our region of interest. A consistent and homogeneous dataset over many years should be the best starting point when trying to determine if modulations of significant wave height due to tides and currents is taking place in the area, independently of the effect of sea ice. The Sea State CCI dataset v1⁶⁵ (CCIv1) is used for this purpose. CCIv1 consists of data from 10 satellite missions and is free from discontinuities in the data due to changes in processing or satellite mission. More specific, we use the level 3 processing from CCIv1 where only valid and good-quality measurements from all altimeters are retained. We chose the time period 1992 to 2018 and use the dataset as is without any further along-track processing, as e.g. in⁶⁶. This allows to gather a large dataset of significant wave height satellite observations in the area, when no sea ice is present. The corresponding dataset is used for the analysis presented in section 3.3.

2.2 Model-based data sources

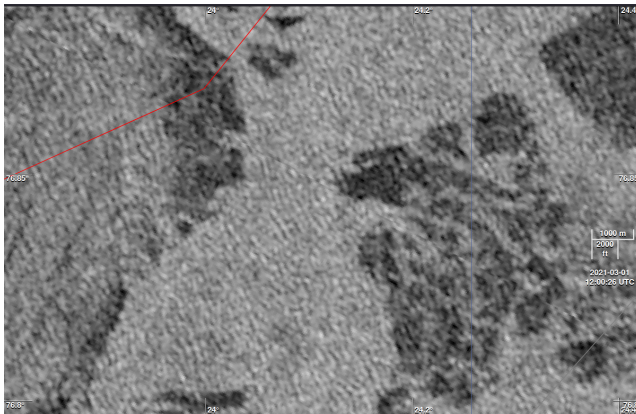
2.2.1 Synoptic view of the ocean and atmosphere conditions in the area of interest

A synoptic view of the situation at 2021-03-02T12Z is presented in Fig. 7. To make the synoptic view as interactive as possible, and offer more exploration freedom than what is allowed by presenting a few static plots, the view is generated using the Ocean Virtual Laboratory (OVL) online tool, and the users can follow the permalink <https://odl.bzh/gVOsfRnq> (accessed November 2023) to access the same map and be able to move forward and backwards in time, as well as switch on and off different map layers (note that minor cosmetic differences are present between the permalink and what we display here, see the rendering parameters description in Appendix). The map presented in Fig. 7 shows the Svalbard area where the buoys are drifting, together with layers reporting (i) interactive markers representing the wind, (ii) the local sea ice concentration obtained from the ARTIST Sea Ice (ASI) algorithm on the AMSR2 sensor of the JAXA GCOM-W1 satellite (data provided by Institute of Environmental Physics, University of Bremen^{67,68}), (iii) the total significant wave height obtained from the global wave model MFWAM of Météo-France with ECMWF forcing and satellite data assimilation^{69,70}, (iv) the direction and SWH associated to the swell first partition, also obtained from MFWAM. We encourage the reader to view the synoptic map interactively online following the permalink provided above to observe the conditions at neighboring times.

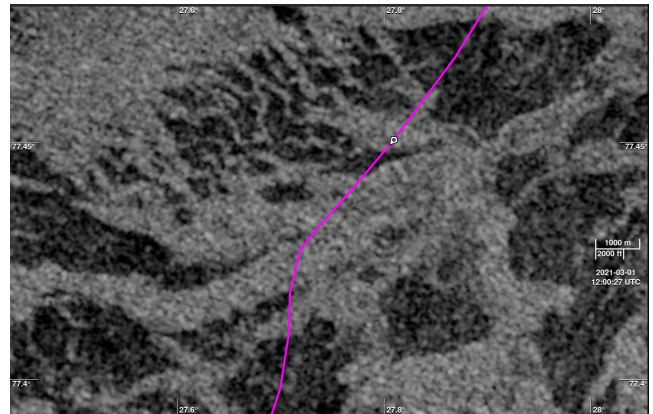
As visible in Fig. 7, the permalink, and in good agreement with Fig. 1 and Fig. 4, the BOIs are well into the ice area during the SWH modulation event. The local wave conditions are dominated by incoming swell, originating from the South West, that propagates through an open water opening before penetrating the sea ice. The wind comes mostly from the North which is covered by sea ice, and, therefore, we expect little locally generated wind wave contributions in the sea ice. The map is generally representative of the situation over the time extent of the SWH modulation event reported, though the SWH of the incoming waves varies in time (but with a much slower typical SWH variation timescale and without the 12-hour modulation we observe in the sea ice), and the direction of propagation of the swell first partition shows minor fluctuations.

Sudden, large amplitude changes in the temperature of the ice, usually caused by changes in the air temperature above, can also influence sea ice mechanical properties and wave in ice propagation and damping. Therefore, we also consider the 2-meter

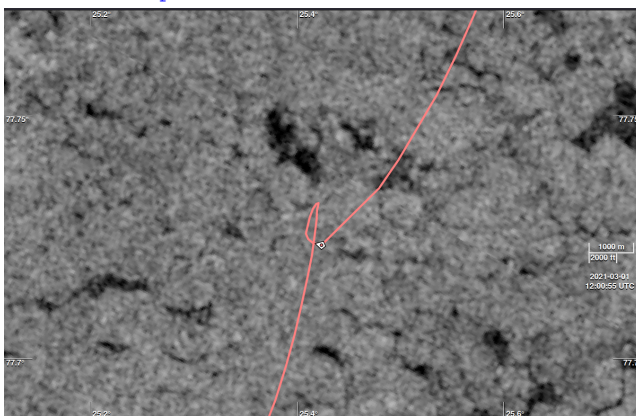
¹github.com/bohlinger/wavy



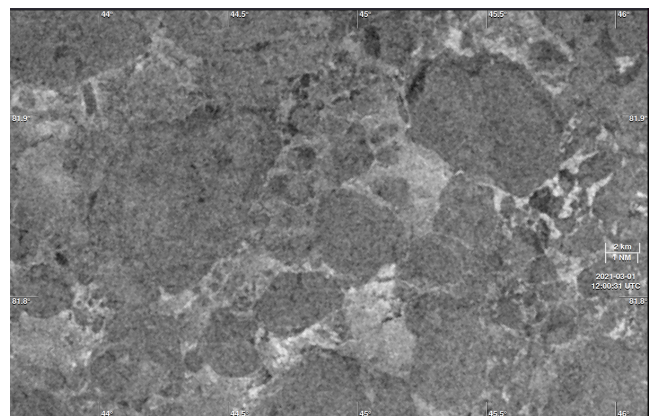
(a) SAR image from the outer MIZ, over the ice tongue South West of the BOIs between Hopen and Svalbard, through which the dominant incoming swell waves travel on their way to the BOIs. Permalink: <https://odl.bzh/oeWZ8UtD> .



(b) SAR image from the outer MIZ, in the neighborhood of buoy 19643 (marker indicates position at 12UTC), South from the BOIs. Permalink: <https://odl.bzh/0j3fBx8k> .



(c) SAR image from the area around BOI 19648. The position of the BOI 19648 at 12UTC is indicated by the marker. Permalink: <https://odl.bzh/JBYRiR6-> .



(d) SAR image far North from the area of the BOIs, where clear unbroken ice floes with typical size $O(1-10\text{km})$ are present. Permalink: https://odl.bzh/M1wrLH_v .

Figure 6. Selection of illustrative SAR images zoom-ins acquired on 2021-03-01 at around 12UTC in the general area of the buoys (except for subfigure (d), which is much further North). The outer MIZ (subfigures (a) and (b)) presents a mixture of areas of broken floes and open water leads. The relatively high sea ice concentration and the limited extent of the open water leads implies that the fetch available for wave development under the influence of wind quickly becomes negligible into the sea ice. Waves are clearly seen propagating from the South West over the ice tongue (subfigure (a)), as also observed in the models (see sections below). By contrast, the ice concentration around instrument 19648 (subfigure (c)) is high, however, many smaller leads, cracks, and a lot of complex structure is visible in the SAR images. This indicates that the sea ice around instrument 19648 in particular, and the BOIs in general, is not constituted of large homogeneous floes, but of many medium size broken floes (with characteristic size typically smaller than $O(500\text{m})$, i.e., typically comparable to $O(1)$ wavelengths). The fact that there are no large unbroken floes in the neighborhood of the BOIs is especially visible when comparing to areas much further North (subfigure (d)), where large unbroken ice floes separated by a matrix of smaller broken ice are clearly visible.

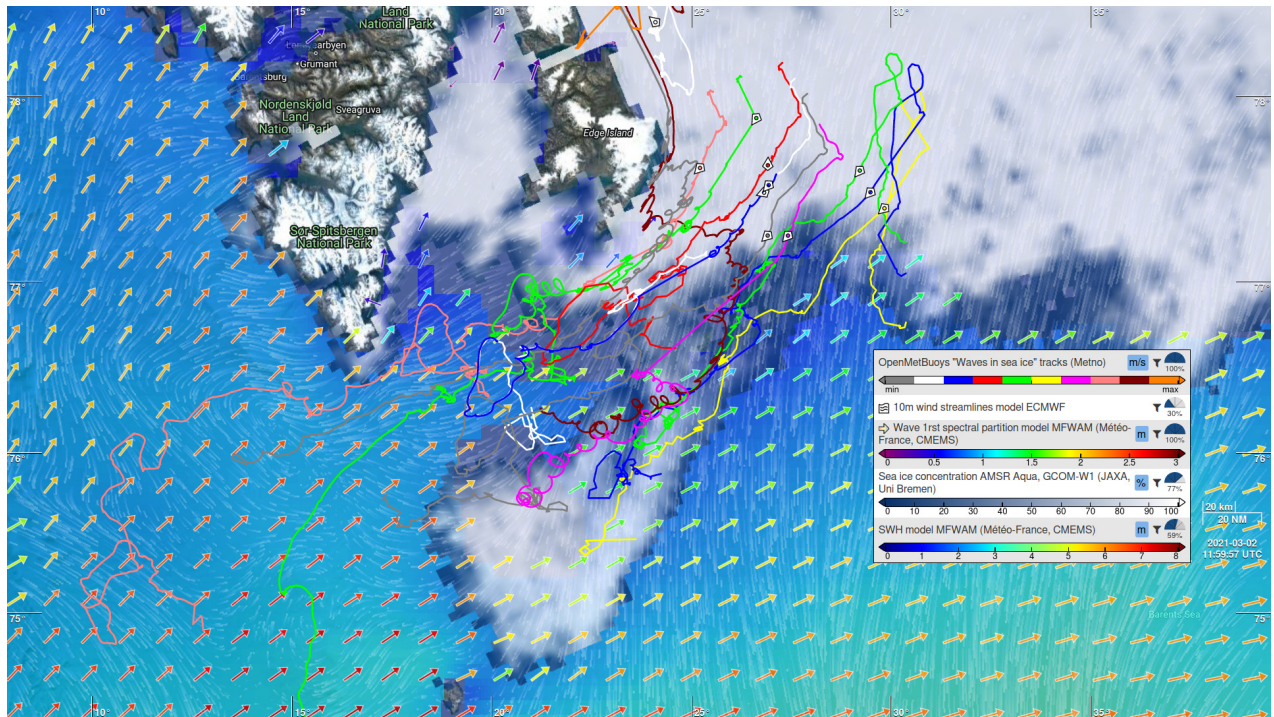


Figure 7. Synoptic overview of the conditions in the area of the buoys during the modulated SWH event. As visible, the buoys (in particular the BOIs) are well within the MIZ (the positions of the buoys taken closest to the reference time 2021-03-02T12Z are indicated with markers). Wind comes from the North and, due to the presence of the sea ice, contributes little to the local SWH. Swell incoming from the South-West is propagating through an open water opening before penetrating the MIZ and propagating to the location of the buoys. This figure is representative of the synoptic conditions over the time extent of the wave modulation event. The data can be viewed interactively online by following the permalink: <https://odl.bzh/gVosfRnq> (accessed November 2023). Note that some cosmetic changes were performed using the command line tool and are not available directly from the permalink: see the OVL technical Appendix for more information.

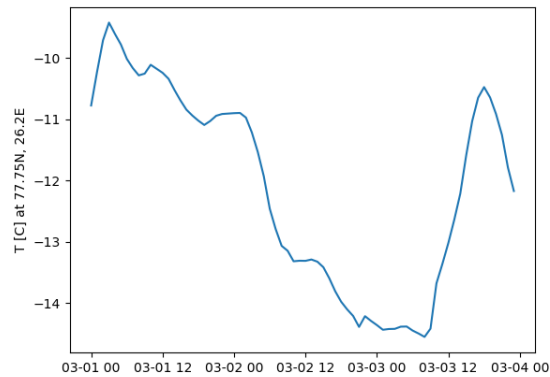


Figure 8. 2-meter temperature in the area of the buoys, as provided by the ERA5 reanalysis. Only moderate temperature changes are observed over the duration of the event. No 12-hour periodicity matching the SWH modulation is observed.

temperature in the area, as provided by the ERA5 reanalysis⁷¹. As visible in Fig. 8, only moderate temperature changes are observed in the atmosphere over the duration of the modulated SWH event.

2.2.2 Custom wave model data in the MIZ during the oscillatory event

In order to investigate if well-known physics, such as wave-current interaction, local wind-wave generation, and established wave in ice attenuation mechanisms, are able to explain for the oscillatory damping we observe, we run a series of custom local spectral wave models in the area of interest. The wave model used is a third generation WAM Cycle 4.7 developed at Helmholtz-Zentrum Geesthacht^{72,73} with modifications made at the Norwegian Meteorological Institute, Norway (MET-Norway). These modifications consist in allowing propagation of waves under the sea ice following the wave attenuation⁷⁴, and a correction of wave-growth in very high winds⁷⁵. The wave propagation in ice-covered areas is modeled by weighting the energy source and sink terms used in the spectral model by the relative sea ice concentration. E.g., the sink term used in the model to represent wave in ice damping is weighted by the local sea ice concentration value (i.e., $SIC_{local}(x,y)$, the sea ice concentration expressed as a fraction between 0 and 1), while source terms arising from winds are weighted by $1 - SIC_{local}(x,y)$. Similarly to the findings obtained in the case sea ice drift by³⁷, this allows for smoother and more realistic representation of the MIZ, compared to what is obtained by setting an arbitrary threshold separating areas where a purely open water vs. sea ice model parameterization is used. The spatial resolution of the model is 2.5 km. The spectral resolution is 24 directions and 30 frequencies with the first frequency equal to 0.034523 Hz. The boundary conditions for the wave spectra come from two sources: the European Center for Medium Weather Forecast when sea ice is included as forcing, and a coarser domain with no ice run at MET-Norway otherwise⁷⁶⁻⁷⁸. The forcing fields used are surface winds from Arôme Arctic⁷⁹, sea ice concentration and thickness from CICE5⁸⁰, and ocean surface currents, which include tides, from ROMS⁸¹.

The domain of interest around the buoys is a coastal area with strong currents and tides, and a natural candidate to the observed modulation could be the effect of wave-bathymetry, wave-current, and wave-tide interaction. Moreover, there are regions of open water South of Svalbard, so locally generated wind waves could also be a potential candidate explanation. Finally, the sea ice in the area is moving under the influence of tides, large scale currents, and winds, which could participate in changing the wave in ice propagation distance, and the resulting wave height observed at the location of the BOIs. In order to take into account these different effects and to investigate the impact of each physical mechanism on the local sea ice dynamics, either in isolation or in combination with each other, different model flavors are run, which we will refer to in the following as:

- W: including the locally generated wind waves, but not the effect of wave-current interaction nor the sea ice,
- WC: including both local wind wave generation and wave current interaction, but not the effect of the sea ice,
- WI: including both wind wave generation and the effect of the sea ice, but not the effect of wave-current interaction,
- WCI: including all 3 effects, i.e. wind wave generation, wave-current interaction, and the sea ice.

Two-dimensional directional wave spectra from the model runs in these different configurations were stored along the tracks of the BOIs.

In addition to the local domain model runs and the current information used therein, timeseries for local tidal information at any specific location in the domain can also be generated. For this, we are using the pyTMD python package^{82,83} to leverage the modal information from the Arc2kmTM Arctic tide model⁸⁴. The Arc2kmTM is a forward barotropic tide model that includes pre-computed maps for the tidal elevation and currents and resolves the influence of 8 principal tidal constituents (4 semidiurnal (M2, S2, K2, N2) and 4 diurnal (K1, O1, P1, Q1)) on a 2km X 2km uniform idealized polar stereographic grid. The area is subject to strong tides due to the features of the local bathymetry, as it has been documented in a number of previous studies taking place in the region⁸⁵⁻⁸⁷.

When more information about sea ice are needed, we use data from the CICE5 model directly, which is run operationally at MET-Norway in the context of the Barents2.5 model and combines the CICE and ROMS models to simulate the dynamics of the sea ice sheet⁸⁸⁻⁹⁰. Bathymetry information is included in these models and taken into accounts in resolving the wave propagation physics. In particular, Barents2.5 uses a 2.5km smoothed (to keep the numerics stable) bathymetry map.

2.2.3 Numerical model of sea ice dynamics

We have already highlighted in Fig. 3 that strong convergence and divergence are present in the sea ice, and that these seem to correlate well with the observed SWH modulation observed at the location of the drifters. The existence of significant patterns of sea ice convergence and divergence dynamics is confirmed by visual inspection of maps of the sea ice convergence from the CICE5 model mentioned above, see Fig. 9. In particular, Fig. 9 confirms that the sea ice divergence and convergence observed from the buoys trajectories is present in the whole area, and shows consistent patterns in space and time. Moreover, we observe that the dynamics and periodicity of the pattern oscillation between a strong state of convergence and divergence matches the 12 hours periods observed in the SWH modulation, corresponding to a dipole-like structure propagating in the sea ice.

In order to further compare these model observations with the BOIs data, the sea ice divergence from the CICE5 model is extracted at the position of the barycenter of the 3 BOIs shown in Fig. 3 (left). The numerical model has some level of noise in both space and time, so we then compute the average between the divergence obtained for the neighboring grid points around the location of the barycenter (taking points that are in a box of ± 1 grid cell around) to get a smoother estimate. The obtained sea ice convergence is part of Fig. 3 (right). As visible there, the model data are in good agreement with the value of the sea ice divergence derived from the observations.

3 Data analysis: what role is played by wave-current interaction, compared to wave-ice interaction, in the modulation observed by the buoys?

In this section, we investigate what categories of physical processes can explain for the waves in ice SWH modulation that we observe. In particular, two categories of mechanisms are candidates to explain our observations as previously highlighted:

- M.1: Wave-current, wave-bathymetry, and wave-tide interaction: these mechanisms are well known for modulating the SWH in areas where strong tides and tidal currents are present. Such a category of mechanisms is independent of the presence or absence of sea ice in the area, and should be observed both in open water and ice covered conditions.
- M.2: Wave-ice interaction and wave attenuation by the sea ice. If this category of physical mechanisms is responsible for the observed SWH modulation, the effect of the sea ice should be a key ingredient in reproducing the modulation observed, and such a modulation should not be observed without the sea ice. This does not mean that the currents and tides do not play a role: for example, the currents and tides may be the physical forcing that cause the changes in sea ice behavior that in turn explains for the modulation observed. However, in such a case, it would be the sea ice, not the tides and currents per se, that would be causing the physics at the origin of the wave attenuation and SWH modulation observations. As a consequence, similar modulations would, in this case, not be observed in ice free conditions.

Our goal in this section will consist in estimating the likely importance and variability of mechanisms belonging to M.1 and M.2 for which we can produce a quantitative estimate, that could be involved in causing the modulation we observe. We will perform such an analysis by relying on both the in-situ data collected, as well as the numerical simulations and models that are available in the area.

We note that the physics at play in both M.1 and M.2 are highly complex, in particular in the Barents Bank where complex bathymetry, tides, and currents are present. Therefore, the following analysis will necessarily rely on a number of approximations and simplifications, and none of them taken individually is a compelling conclusive proof. However, our aim is to compare different approaches, and check if they arrive at the same typical conclusions and order-of-magnitude estimates.

We also want to highlight that some potential mechanisms are well established and can be quantified, while some others are more challenging to estimate. For example, regarding possible explanations belonging to the M.1 category, the models should provide reasonable estimates of wave-bathymetry and wave-current interaction, including the refraction of waves by current gradients, since these are the result of complex but well established physics. Similarly, in the M.2 category, the effect of

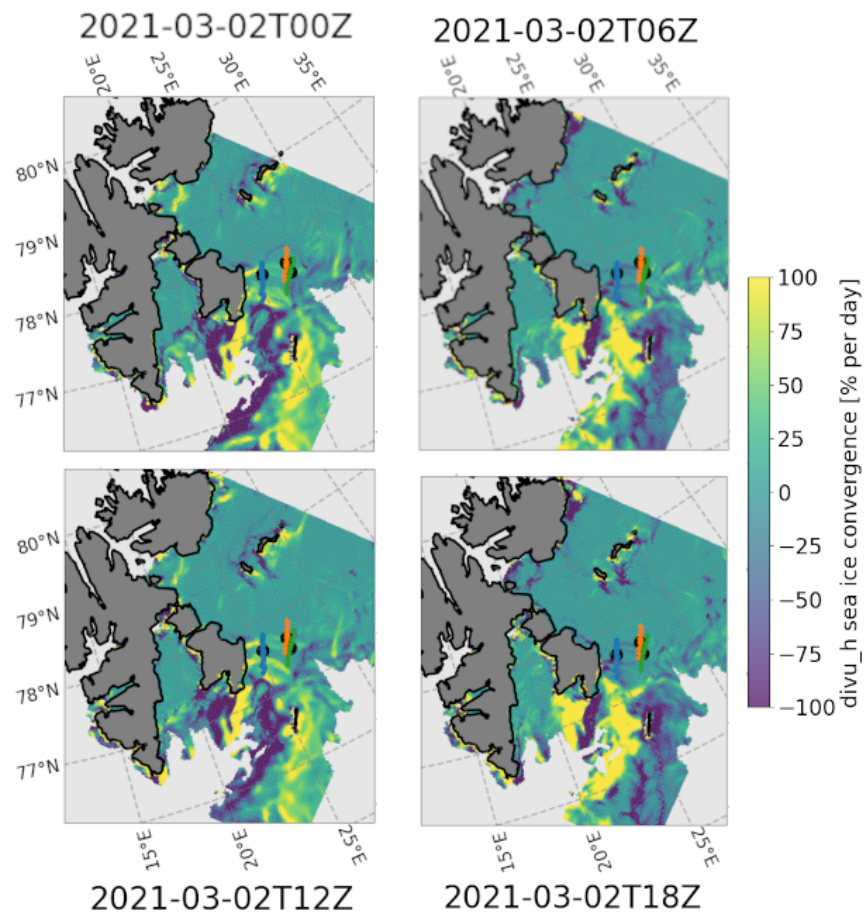


Figure 9. Illustration of the sea ice convergence and divergence pattern in the area of the buoys, as obtained from the sea ice velocity divergence field produced by the CICE5 model output. A clear pattern is visible both in space and in time, with the same 12 hours periodicity as observed in the SWH modulation. Further visualization of the animated video of the sea ice model divergence shows the existence of a dipole that rotates in the neighborhood of the location of the buoys, leading to a periodic transition between phases of sea ice convergence and divergence at any point of the area considered.

MIZ edge displacement under the influence of strong currents and winds, and, hence, increased wave in ice attenuation due to increased wave propagation distance in the sea ice, should be well captured by ice models corrected from assimilated satellite measurements. However, some other mechanisms, like an hypothetical change in the wave in ice energy dissipation following modifications of the sea ice state of divergence and "compactness", cannot be readily estimated from current models.

Therefore, the following analysis can either reveal that a known mechanism belonging to the M.1 or M.2 category is able to explain for the SWH modulation observed at the BOIs, or, if unsuccessful at explaining the observations, that additional physics must be considered.

3.1 Investigation of current-induced wave field modulations using the wave action and wave ray approximations

In this section, we want to investigate how much wave-current modulation can be expected following the influence of tides and tidal currents and their interaction with bathymetry trapping effects, as an order-of-magnitude. For this, we leverage simplified models, including the wave action and wave ray models. While they are not as complex as the full wave models used in the next section, such simplified models provide a good physical and phenomenological understanding of the wave-current modulation phenomena happening in the area. These approximate models should not be taken as a ground truth, as they make many simplifications and approximations, and they neglect important phenomena including, e.g., non-linear interaction. Despite these limitations, they are useful for providing a high level view of the main phenomena.

Wave field modulations due to currents are a combination of local and non-local effects. For instance, the conservation of wave action on quasi-stationary currents causes an increase in SWH on counter-currents that can be considered and computed as a local modulation⁹¹. However, in-situ observations also include the signal of non-local modulations, or simply cumulative effects, since waves are constantly interacting with the local currents along their propagation path⁹²⁻⁹⁴. One such non-local effect is current-induced refraction, which is considered to be the dominating cause in creating spatially dependent wave height variability at scales of kilometers^{95,96}. These effects are both linked to the wave kinematics which are incorporated in spectral wave models. However, simplified theoretical considerations are helpful in determining their relative contributions⁹⁷.

When considering the local wave action effect on SWH, the deep-water modulation in wave amplitude a for a steady current having the same (resp opposite) direction to the wave propagation direction can be expressed as⁹⁸

$$\frac{a}{a_0} = \frac{c_0}{\sqrt{c^2(1 \pm \frac{2U}{c})}}, \quad (5)$$

where c is the wave phase velocity, U is the current speed, the subscript $_0$ denotes the wave amplitude and celerity value when $U = 0$, and the \pm value corresponds to current having the same, resp. opposing, direction as the waves. Here, the wave celerities c_0 and c are related quadratically through the Doppler shift equation⁹⁸: $c/c_0 = (1 + \sqrt{1 \pm 4U/c_0})/2$. In our case, the current field has a strong tidal signal and the maximum current speeds in the vicinity of the BOIs are typically about 0.4 m s^{-1} (this value can be either extracted from the Barents2.5 model output [not shown], or from pyTMD and the Arc2kmTM model, see the Fig. 15, noting that slightly stronger tides can be obtained at some other locations in the area of interest than what is presented there). The energy modulation according to Eq. (5) is sensitive to the wave celerity, and thus wavenumber, such that longer waves are less modulated than shorter waves for a given current speed. Consequently, the amplitude modulation in Eq. (5) for waves with initial periods $T = 8 \text{ s}$ and $T = 12 \text{ s}$, opposing (or following, with a sign change including in the Doppler effect on c) a $U = 0.4 \text{ m s}^{-1}$ current from rest, is about $\pm 7\%$ and $\pm 5\%$, respectively.

To assess the current-induced modulation due to refraction along the propagation path of the waves, we perform a ray tracing analysis using the solver by⁹⁹. Currents are taken from the Barents 2.5km ROMS model mentioned above, and fully allowed to vary in time during the wave ray propagation. Propagation paths are found to be very sensitive to their initial direction and location, which is a well known fact for this kind of simplified models¹⁰⁰. Therefore, we establish a representative ensemble of wave rays by perturbing the initial direction θ_0 two times in the relative positive and negative angle direction, following the typical amount of directional spread present in the incoming wave spectrum. Furthermore, we also included the wave periods $T \in [10, 11, 12, 13, 14] \text{ s}$, to include, similarly, the frequency spread of the incoming waves. Consequently, the ensemble was created in order to be representative to the WAM directional wave spectrum and consistent with what is presented in Fig. 12. The full ensemble consisted of 40 (initial propagation times) \times 5 (ensemble representing wave directional spread) \times 5 (ensemble representing wave periods spread) = 1000 wave ray realizations. A subset of the results are shown in Fig. 10 for illustration purposes. It is clear that the longest waves are sensitive to the bathymetry, which can act locally as a wave guide and trap these. In such cases, the ambient current may increase the spreading of the wave rays such that additional rays gets caught by the bathymetry. However, the wave rays are not always spread more due to the tidal currents since current-induced refraction depends on the vorticity of the ambient current along the wave ray propagation direction¹⁰¹, which changes in time along the wave ray track.

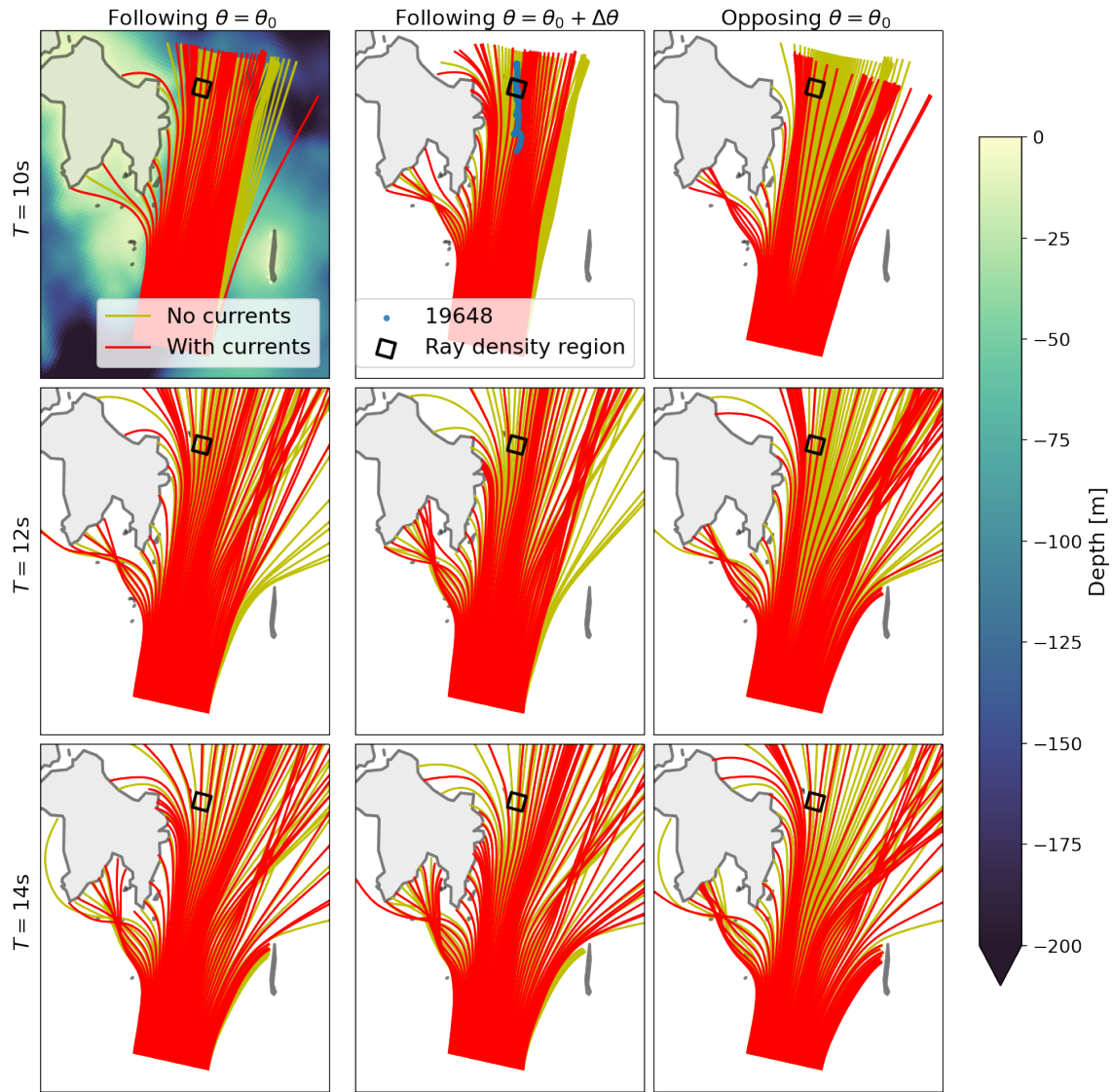


Figure 10. An illustrative subset of the 1000 ensemble wave ray simulations performed. Results are shown with (red) and without (yellow, used as a baseline) current forcing. Rows from top to bottom show the ray paths for 10s, 12s, and 14s period waves, respectively. Columns from left to right show (i) wave rays corresponding to the average wave direction (θ_0) for an initial propagation time corresponding to waves following the currents, (ii) wave rays corresponding to one of the perturbed wave directions ($\theta_0 + \Delta\theta$, where $\Delta\theta$ is a deviation from the average wave direction) for an initial propagation time corresponding to waves following the currents, (iii) wave rays corresponding to the average wave direction (θ_0) for an initial propagation time corresponding to waves opposing the currents. Note that the currents evolve in time as the wave rays propagate. The track of BOI 19648 is shown in the upper middle panel, together with the black square indicating the region for the wave ray density analysis. As visible across the figure, the exact refraction of the waves is sensitive to both the current conditions, the wave period, and the exact wave direction. As a consequence, while individual ensemble members may give strong modulation effects, their averaging partially cancels out (see further discussion and analysis of this aspect in Fig. 11).

Wave ray density is representative of the amount of wave energy (i.e., the square of the SWH) that is obtained in a given area at the corresponding time. Therefore, the wave ray density can be used to derive a proxy estimate for the SWH modulation obtained due to wave-current-bathymetry interaction. More specifically, we perform a normalized wave ray density analysis for a $12.5 \text{ km} \times 12.5 \text{ km}$ region along the track of BOI 19648 (upper middle panel Fig. 10). Here, we count the number of rays within the region and normalize it on the number of rays within the same region, obtained in an additional baseline case without currents (i.e., the baseline case only takes depth-induced refraction into account). As a consequence, this quantifies the amount of modulation introduced in the corresponding region. The relative ray density square root (RDsr_r) is computed as:

$$\text{RDsr}_r = \sqrt{\frac{\text{RD}_c}{\text{RD}_{nc}}}, \quad (6)$$

where subscripts r , c and nc denote quantities that are considered as relative, with current, and without current, respectively. We take the square root since the wave action density propagates along rays and is proportional to the square of the wave amplitude a , while the observations correspond to a measure of the SWH, which is linearly related to the wave amplitude.

The time series evolution in RDsr_r averaged over all ensemble members for the region of interest, is shown in Fig. 11c. As mentioned, there are large fluctuations in the single ray tracing realizations (Fig. 11b, d). These fluctuations are filtered out when averaging over the directional and frequency spread representative of the incoming wave conditions (Fig. 11a). The average over all the directions and wave periods shows a clear tidal modulation, which translates into a SWH modulation of around 20–25 % (Fig 11c). Therefore, we expect refraction to play an important role in the wave field modulation. The analysis presented here does not take into account important dynamics like non-linear wave-wave interactions and wave attenuation, and is, as a consequence, only a typical order of magnitude estimate. Moreover, the ray theory approximation is known to fail at focal points and at caustics, in which case, wave phases and local interference patterns need to be considered¹⁰². However, such patterns are usually observed in very localized areas (typically covering a spatial extent just a few wavelengths), so that this explanation is incompatible with the fact that similar modulation is observed at the 3 BOIs separated by several tens of kilometers (see Fig. 3 for an overview of the distances in km between the 3 BOIs).

Therefore, our analysis suggests that we can expect a tidal signal in the modulations, which agrees qualitatively with the modulations in the swell 1 partition from the spectral wave model (see next section, Fig. 13). However, the modulation level expected due to wave-current interaction is by far not enough to explain the observations by the BOIs presented in Fig. 2.

3.2 Numerical models analysis of the effect of bathymetry, currents, and tides on significant wave height

Our objective in the present section is to determine whether wave-current interaction, or simple sea ice dynamics (such as sea ice drift leading to a change in the wave in ice propagation distance) can explain for the modulation observed, according to advanced, state-of-the-art numerical model runs that include the wave-current interaction and estimates of the sea ice attenuation. Compared with the wave ray analysis in the previous section, these models include additional physics (such as non-linear interactions, and dynamics of the full wave spectrum during wave propagation).

A subset of the directional spectra obtained from the different model runs along the trajectory of BOI 19648 are presented in Fig. 12. The sea state was bimodal for all the wave model runs. Compared to the results presented in Fig. 7, the main dominating swell propagating from the South-West towards the North-East is well reproduced. In addition, the model reveals a secondary lower amplitude slightly higher frequency swell signal propagating towards the North-West, which was not visible in Fig. 7, since only the dominating swell component was shown there. The shorter wind-waves frequencies are, as expected, not present in the model runs including sea ice effects, due to both the attenuation effect by the sea ice, and the fetch blocking effect of the sea ice that prevents wave growth in ice covered areas since the wind is generally blowing from the sea ice towards the open ocean during the period considered. In order to quantify the current-induced modulation on the different components in model runs without sea ice, we perform a spectral partitioning in direction, since the dominating directions were more or less stationary throughout the study period (not shown here). The swell components within the range (330° , 90°) (sector indicated by the red limits on one of the directional spectra at Fig. 12) are hereinafter denoted as ‘‘Swell 1’’, and will be used when analyzing model outputs without sea ice included (i.e., model outputs from W and WC runs), since the dynamics of the swell-current interactions of interest here are otherwise hidden in the locally generated wind wave signals that are forced in the models in the absence of ice.

The temporal evolution in SWH obtained by integrating over the directional spectra, along the position of the BOI 19648 (which is furthest into the sea ice and shows the strongest modulation) where these are taken, for the W, WC, WI, and WCI cases, are presented in Fig. 13. For cases without sea ice, only Swell 1 partition is considered as discussed above. For cases with ice, the whole directional spectra is considered. Several interesting aspects are visible there.

First, the Swell 1 partition in the models without sea ice (W and WC) predicts far too high SWH at the location of the instrument, as expected. If we add the wind sea and secondary swell component, the SWHs for the models W and WC would

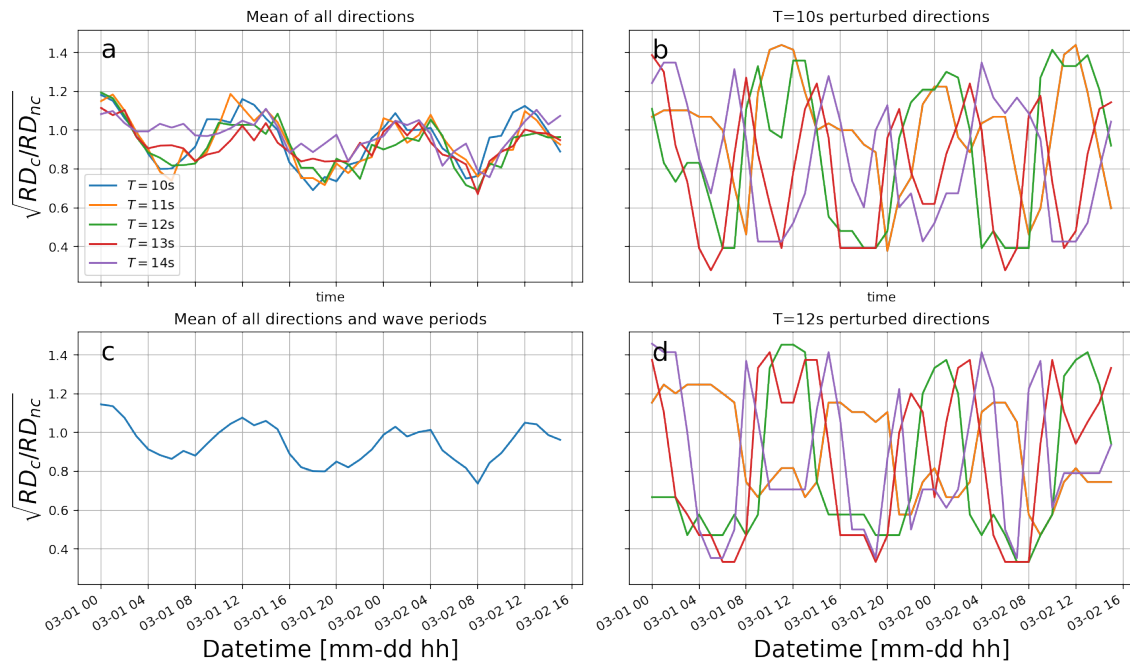


Figure 11. Estimates of the expected SWH from wave ray density analysis. Panel a) shows the expected SWH modulation at the location of the BOI 19648, averaged over directions for each frequency used in the rays ensemble, respective to the baseline case without currents. Panels b) and d) show wave ray analysis predictions at the location of the BOI 19648, obtained by perturbing the propagation direction at a fixed frequency. This illustrates the sensitivity of the wave ray dynamics to the ensemble member parameters. Panel c) shows the mean normalized ray density RD_{sq_r} prediction following the track of BOI 19648, obtained by averaging over the ensemble respectively to both frequencies and directions, which is our best estimate for the expected SWH modulation following the wave ray analysis.

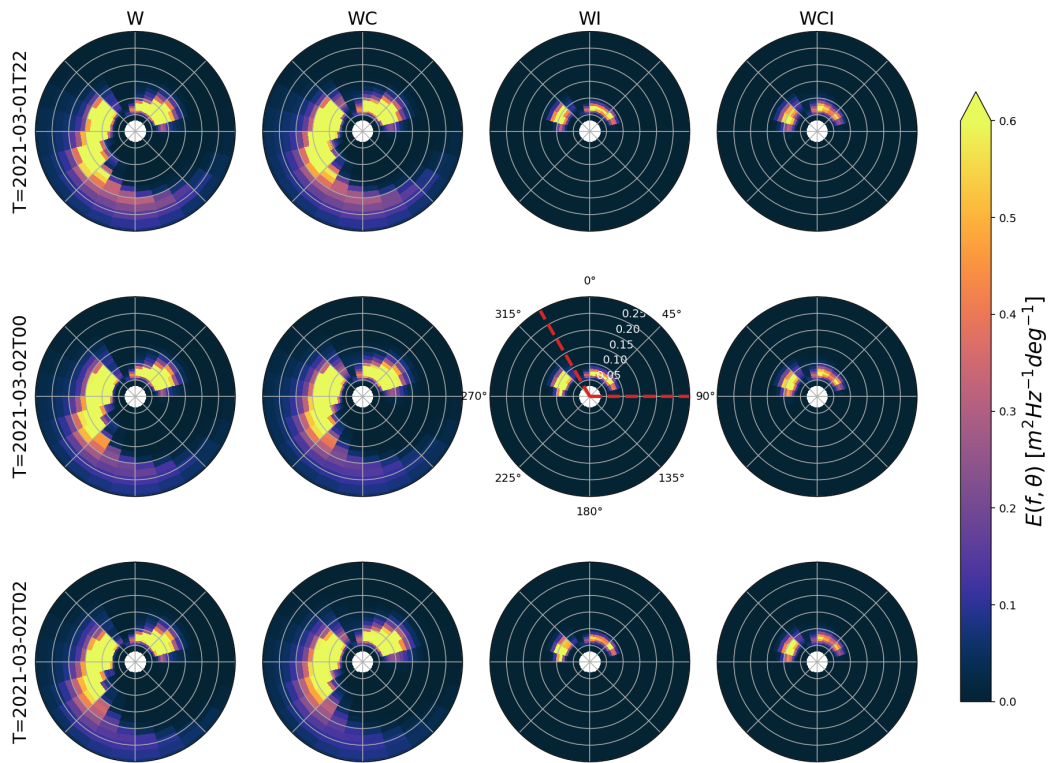


Figure 12. Directional spectra from the custom WAM model runs. Columns from left denote W, WC, WI, and WCI model runs, respectively, while rows from top denote the temporal evolution with steps of 2hrs following the track of the BOI 19648. Red lines in the middle panel in the WI column denote the sector for the swell components that undergoes most tidal modulations due to currents, and are thus used for the spectral partitioning "S1".

be about 1–2 m higher than what is observed at the BOI 19468 throughout the period (not shown). The higher SWH obtained in model runs without the sea ice is of course expected, as the sea ice induces a strong energy dissipation, resulting in attenuation of the waves. This effect is naturally not included in the W and WC cases.

Second, model runs with sea ice attenuation included (WI and WCI runs) produce qualitatively reasonable SWH values in the MIZ at the location of the instrument, except for the "modulated" attenuation effect that is not reproduced. This is interesting on two aspects: first, it indicates that the waves in ice attenuation parameterization used, which was not tuned specifically for the present case but used default values from⁷⁴, is reasonably effective at capturing the typical intensity of the wave in ice attenuation effect, and the resulting SWH at the location of the BOI 19648. Second, it shows that, while the case we study displays strongly modulated SWH values, the modulation we observe is likely an additional effect that comes on top of the wave attenuation mechanisms that are robustly captured by the established attenuation parameterizations.

In order to estimate the impact of the wave-current interaction on the SWH predicted by the models, we compute the relative difference between model runs with and without wave-current interaction, defined as:

$$R_{WC(I),W(I)} = \frac{SWH[WC(I)] - SWH[W(I)]}{SWH[W(I)]}, \quad (7)$$

where the case pairs without (WC vs. W) and with (WCI vs. WI) the ice effect are considered. We find that the modulations calculated for the SWH are mostly between 10 %–30 % for both W against WC (using the Swell 1 partition), and WI against WCI (upper panel Fig. 13). Such relative differences are similar to what is reported elsewhere in terms of current-induced modulations intensity^{103, 104}. This 12h modulation is less evident when considering the wind sea part as well as the full spectrum in the WC vs. W case, indicating that the swells propagating across long distances and that do not receive a locally generated energy input are the most affected by the current modulation effect.

Finally, since (i) we observe that no or only little modulation is present in the WI and WCI cases, and (ii) the sea ice input is provided by the CICE5 model which includes sea ice drift, melting, and freezing, as simulated by a numerical model and corrected by assimilated satellite data, we conclude that simple sea ice changes, such as large displacements in the MIZ edge, or rapid changes in the sea ice thickness, are unlikely to be the cause of the SWH modulation we observe. Indeed, these effects should be, if not perfectly, at least reproduced overall by the WI and WCI model runs.

These results suggest that, according to the numerical model runs, the observed SWH modulation observed by the buoys, which shows a modulation ratio of up to 90% as previously highlighted, cannot be explained by the wave-current interaction (which is predicted to be at least 3 times smaller even when it is at its strongest), nor by simple sea ice dynamics included in present sea ice models and wave in ice attenuation parameterizations. Moreover, the modulation observed in the sea ice due to the wave-current interaction is only around 5-10% when the strongest modulation ratio is observed from the buoys around 2021-03-02T00:00 to T 06:00, which is an order of magnitude weaker than the modulation measured by the buoys. While this is not an absolute proof that wave-current interaction cannot explain for the observations we report, since numerical models are not perfect, this is an evidence going in this direction. The wave-current modulation obtained in the models, which is typically 10–30% at most, is also typically in agreement with what has been observed at other locations away from the shore, where strong tidal currents are present^{103, 104}.

3.3 Analysis of significant wave height satellite observations in ice free conditions, and correlation with tidal signal

In order to further investigate if the SWH modulation observed could arise from the effect of wave-current and wave-tide interaction per se independently of the presence of the sea ice, we look into the direct satellite altimeter observations of the significant wave height in ice free conditions gathered by the wavy package, and we compare these to the corresponding tide information generated from the pyTMD package and Arc2kmTM model described above. The underlying idea is that, if the modulation we observe is due to the wave-current or wave-tide interaction per se and is independent of the presence of sea ice, it should then be observed also by the satellites measuring the local SWH in the absence of sea ice.

Ideally, we would like to gather a dataset of N pairs of SWH observations, $(SWH_+, SWH_-)_i, i = 1..N$, with both observations in a pair being obtained with a 6-hours time difference for a variety of different tide phases, so that the SWH at the tidal phase corresponding to maximum and minimum of the SWH following wave-current interaction can be obtained. One could, from such a dataset, compute the average modulation ratio $R = \left\langle \frac{SWH_{+,i} - SWH_{-,i}}{SWH_{+,i}} \right\rangle_i$, where $\langle \cdot \rangle_i$ means "average over sample pairs i ", $+$ and $-$ refer to the time when maximum and minimum SWH are obtained due to the wave-tidal currents interaction, and R is the SWH modulation ratio due to tidal currents (which can be turned into a percentage by multiplying by 100 for convenience). To make sure that similar wave-current conditions are performed, one could, if enough such pairs are available, limit such an analysis to wave conditions that present similarities in spectrum direction and frequencies with the current case. Unfortunately, since there is no long-term in-situ buoy data available at the location of interest, and satellite observations we know of in this

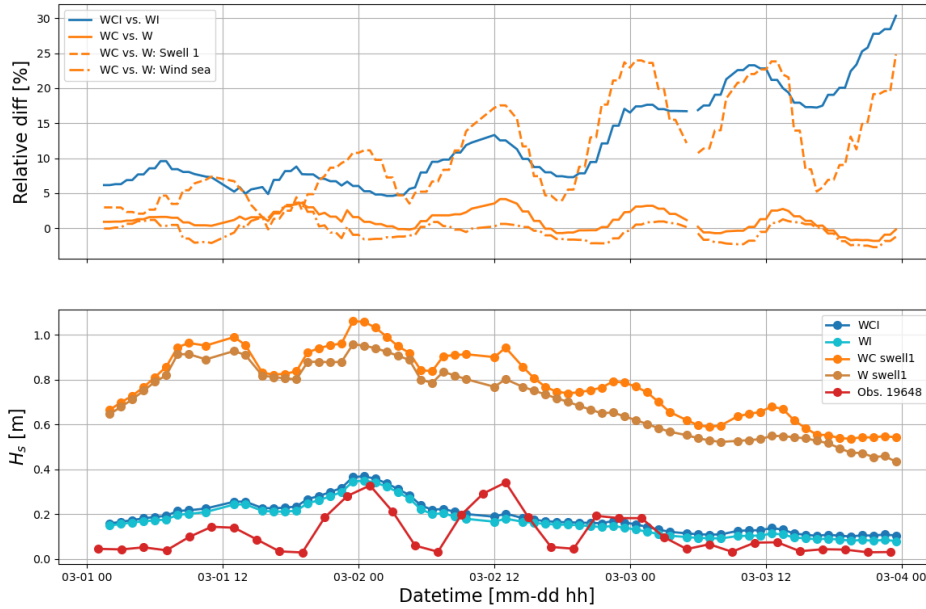


Figure 13. Temporal evolution in SWH (lower panel), and the relative difference due to the effect of currents (upper panel), for the WAM wave model runs. Different model runs, with (if the letter is present in the run case) or without Wind energy input (W), Current effects (C), and Ice effect (I), and combinations of these, are presented following the track of the instrument ID 19648, which is the instrument deepest into the MIZ, and has highest time resolution. Relative differences are computed using Eqn. (7) for WI vs. WCI (blue line), WC vs. W (orange line), Swell 1 of WC vs. W (dashed orange line), and the wind sea component of WC vs. W (dash-dotted orange line). The WAM model is able, overall, to reproduce the envelope of the SWH attenuation by the MIZ. However, the wave in ice modulation effect measured by the buoys, with an observed modulation ratio of up to 90%, is not reproduced by the model runs. The effect of currents, both with and without ice, is limited to a modulation of the SWH within 5–30% of the no-current value (W vs. WC, and WI vs. WCI runs). During the strongest modulation phase (2021-03-02T00:00 to T 06:00), a modulation ratio of 90% is observed by the buoy 19648, while the wave-current interaction computed by our model induces only a 5–10% modulation. Note that the strong increase in the relative difference at the end of the timeseries may, to some extent, be amplified due to the reducing baseline SWH value, which corresponds to a reduction of the denominator in Eqn. (7).

area have a repeat rate significantly slower than the 6 hours that this direct approach would request (and a 6 hours repeat rate would be the absolute lowest bound: in order to gather 6-hours pairs of observations covering different tidal phases, an even higher repeat rate would actually be needed), this method is not directly applicable.

Therefore, we instead leverage our dataset of direct satellite observations by performing a linear regression between the SWH measured by the satellites and the tidal currents obtained from the Arc2kmTM tide model. Our goal is to compute an estimate of the typical average intensity of the tidal current-induced SWH modulation that can be expected for the average representative incoming wave spectrum and SWH conditions obtained in the area. This is not a perfect approach, since one can expect the actual modulation observed at any time to be dependent on the incoming wave directional spectrum, including its direction and peak frequencies properties, as previously mentioned. However, this can still provide an indication of the typical magnitude of the tide-induced open water SWH modulation effect to be expected. Moreover, since the location considered is close to the coast, the direction for the incoming waves is mostly limited to incoming from the South South West and the Norwegian sea (as we observe in our dataset), or the South South East and the East Barents sea; other directions do not have the fetch necessary to produce significant swells, due to the close proximity of coastlines and the sea ice edge. This approach also assumes that the SWH modulation effect is, in first approximation, linear relative to the incoming SWH value so that a linear model captures the averaged variability; we believe that this linearization hypothesis is reasonable in first approximation to get a proxy estimate.

In order to perform this regression analysis and check that it is robust to the details of the choice of the exact collocation area, we select a set of local areas around the position of the buoy with ID 19648 during the event, with different spatial extents for the collocation box width, ranging from 30 to 60 km. Such relatively large boxes (relatively to the footprints of the satellite measurements, which are typically on the order of 1-10km depending on the satellite and its embarked instrument) are needed to obtain enough collocations to obtain reasonable statistical averages. The most representative such box, corresponding to a side of 45km, is presented in Fig. 14 (left). The center of the boxes is chosen so that the trajectory of the BOI 19648, which shows the strongest SWH modulation, is well covered. For each of these collocation boxes, we find all measurements from satellite altimeter observations obtained from the wavy package that are within the corresponding areas, resulting in sets of satellite collocations SWH measurements $\{SWH\}_d$, with d the collocation box size within the set $\{30, 35, 40, 45, 50, 60\}$ kms. We then compute the tidal currents at the middle of the box for each collocation time, using pyTMD and the Arc2kmTM model data, resulting in the sets of predicted tidal current values. We make the choice of using the middle of the areas for all tidal calculations both for simplicity, and because extracting and computing the tidal modes using pyTMD and Arc2kmTM is relatively expensive computationally if many different spatial locations are considered. Since the boxes are relatively small relatively to the typical spatial scale for the tide amplitude and phase variability, the resulting mismatch is small, in particular regarding tidal elevation and current phase variations within each local area, as illustrated in Fig. 14 (right), which compares the pyTMD tidal prediction at the center of the 45 km box to the tidal prediction obtained at the locations following the displacement in time of the BOI 19648.

From these data, we can then compute, for each box side d , the linear regression between the tide current estimates from pyTMD and the satellite SWH observations. This linear regression analysis is valid for the statistically averaged ice free wave conditions in the area:

$$SWH_{average} = SWH_0 + \alpha_{u,v} pyTMD_{u,v}, \quad (8)$$

where $SWH_{average}$ indicates the statistically averaged SWH in the dataset observed for given current conditions, $\alpha_{u,v}$ represents, for the same average SWH conditions, the linear variability of the SWH observed as a function of the tide currents, and $pyTMD_{u,v}$ represents the tidal current estimates obtained from pyTMD. Either u or v , which indicate the tidal currents in the East-West and North-South directions, respectively, can be used to perform the regression. Since, as visible in Fig. 14 (right), the tidal conditions in the area correspond to a propagating wave where the currents and tide elevation are at first approximation in phase and proportionally scaled versions of each others, the difference between both choices remains moderate.

Based on this estimate, the typical average modulation ratio for each box width d , obtained for ice-free waters in the statistically averaged wave conditions sampled by the satellite measurements, can be obtained as:

$$modulation_ratio_{u,v} = \frac{SWH_{max_modulation} - SWH_{min_modulation}}{SWH_{max_modulation}} = 1 - \frac{SWH_0 + \alpha_{u,v} \min(pyTMD_{u,v})}{SWH_0 + \alpha_{u,v} \max(pyTMD_{u,v})}, \quad (9)$$

where we assume that α is positive (if α is negative, the signs in front of α and use of min and max should be switched).

Results for the modulation ratio are presented in Table 1. At this point, we want to insist again that these results are statistical averages, obtained based on satellite observations, that present the typical amount of tide-induced SWH modulation for the statistically averaged local wave conditions, based on a linear regression analysis. Moreover, the correlation is performed

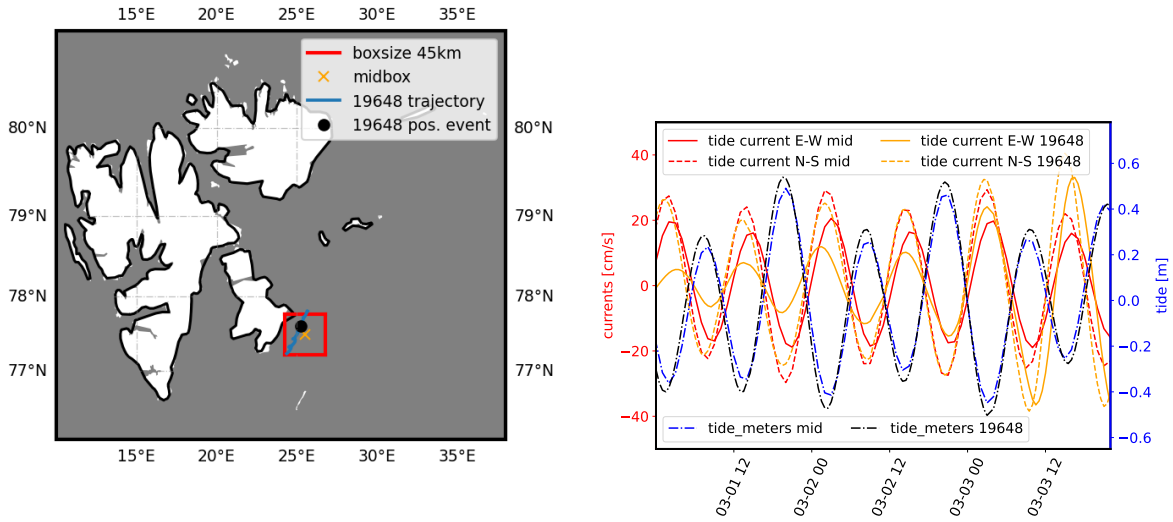


Figure 14. Left: illustration of the 45km-width box used to select satellite data SWH measurement collocations. The box contains the trajectory of the BOI 19648, which is deepest into the MIZ and shows the strongest SWH modulation ratio. The position of the instrument 19648 during the most intense modulation event is indicated by the black dot, and is close to the middle of the box which is indicated by the cross. Right: illustration of the tide currents and elevation at the center of the box ("mid" quantities), compared to the ones obtained following the trajectory of the instrument ID 19648 ("19648" quantities). The signals phases and order of magnitude for their obtained amplitudes is similar between the two, indicating that the box extent is correctly chosen. Naturally, the sign of the currents depends on the choice of the referential axis (here, East-West for u and North-South for v), so the apparently opposed phase between tide and current has no particular physical meaning.

based on local tidal information, while effects happening along the wave propagation may also play a role and be out of phase with the local tide and currents signal. This means that these results should be taken only as a proxy, or an order of magnitude estimate, for the tide induced SWH modulation effect to expect in the area. Specific cases may result in different values, but the results presented in Table 1 can be expected to give an estimate of the typical modulation intensity to be expected in average.

Despite these methodological limitations, the values presented in Table 1 are typically consistent with the findings presented in the previous section, including the results shown in Fig. 13. A typical statistically averaged modulation of 20-30% is obtained from our analysis, which corresponds well to the relative differences found above. This would indicate, similarly to the findings from the previous section, that the wave-tidal current interaction per se is unlikely to explain for the modulation we observe from the BOIs. This is also similar to the typical amount of modulation reported in other areas such as, e.g.,¹⁰⁵.

We have applied a scaled version of Eqn. 8 to the specific modulation case observed at the BOI 19648. By scaling the SWH and SWH modulation obtained in Table 1 to match the peak SWH obtained for BOI 19648, and computing the tide from pyTMD at the exact positions reported by its GPS track, we can compute the statistically averaged wave-tidal current modulation expected for the SWH reported by BOI 19648. Results are presented in Fig. 15. As visible there, and in agreement with the discussion above, the SWH modulation observed is not explained by the statistically averaged tidal current effect. Moreover, the phase of the modulation obtained from the linear regression analysis applied to the predicted tide at the location reported by the GPS track for BOI 19648 is also partially mismatched with the SWH modulation observation. While we acknowledge that our tide current estimates are imperfect as they are obtained from a numerical model with a finite resolution, we consider that this is an additional evidence that another mechanism is likely to explain for the observed SWH modulation. We also observe that the tidal currents amplitude at the location following the track of instrument 19648 increases towards the end of the event, which is in agreement with the findings in Fig. 13 that a stronger current induced modulation is obtained towards the end of the timeseries.

Box width d (km)	number of satellite collocations	linear regression expected SWH modulation ratio (%), u	lin. reg., v (%)
30	825	25	28
35	1106	24	26
40	1451	28	26
45	1772	22	27
50	2175	24	28
60	3091	25	29

Table 1. Summary of the linear regression analysis between local tidal currents produced from pyTMD using the Arc2kmTM model, and satellite observations collected using the wavy package of the SWH in a box of width d around the area of interest. Enough collocations are obtained to derive statistically significant modulation ratio values. The modulation ratio values derived are roughly similar when derived from either the u (E-W) or v (N-S) current components of the pyTMD tidal current estimate, which is consistent with the observation from Fig. 14 (right), that the local tide signal is dominated by a propagating wave, with both u, v, and the tide elevation moving in phase. The typical modulation ratio observed is between 20 and 30%. The standard deviation uncertainty on the regression slope, and, therefore, on the SWH tide-driven modulation ratio, is typically within 15% of the estimates obtained (not reported here), which confirms the confidence in the values of the statistically averaged modulation ratios presented. The modulation ratio found shows no strong dependence on the box width, which confirms that the analysis is not overly sensitive to this parameter. The table columns indicate the box width used for each analysis, the number of satellite collocations obtained for the corresponding box width, and the SWH modulation ratios derived using Eqn. 9 based on either the u or v tidal current components, respectively.

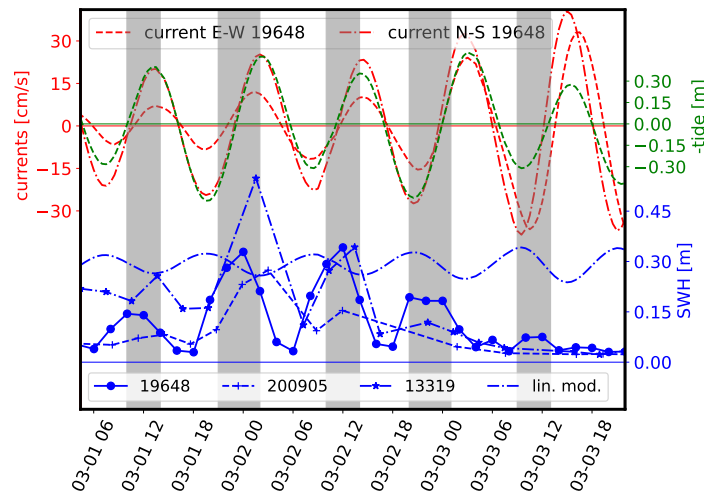


Figure 15. Application of the linear regression analysis results to the BOI 19648. The tidal currents and tide elevation following the position of the BOI 19648 (as reported by its GPS track) are computed using pyTMD and Arc2kmTM. Based on this, the linear regression corresponding to Eqn. (8) is scaled linearly to match the peak SWH recorded by the BOI 19648, and the associated statistically averaged modulation in the area is computed (indicated by the "lin. mod" curve). The obtained linear modulation is not able to reproduce the observation reported by the BOI 19648 in the neighborhood of the strongest modulation event (03-01T12 to 03-02T18). This indicates that the modulation observed at the BOI 19648 does not match with the statistically averaged tide-induced modulation observed by performing a linear regression locally in the area, which suggests that another mechanism is possibly the driver for the modulation observed at BOI 19648.

4 Discussion: what wave-ice interaction physics and mechanisms are likely explanations for the waves in ice modulation observed?

A natural first candidate for explaining the 12-hour period SWH modulation observed at the BOIs is the effect of tide and tidal currents on the wave field, due to either wave-current interaction, induced water depth changes, or more exotic effects such as increased turbulence levels in the ocean following the passing of the tidal wave, leading to a subsequent increase in wave energy dissipation.

However, a detailed analysis including a combination of wave ray paths, numerical model runs including wave-current interaction, and a correlation analysis between local tides and SWH satellite observations when the ice is absent from the area, indicate that the tidal current can likely only explain for a SWH modulation ratio of typically at most around 30%, well below the modulation ratio of around 90% that we obtain in our in-situ buoy observation timeseries. While numerical models are not perfect, we would expect state-of-the-art models to capture a much larger part of the intrinsic wave-current interaction if this was the dominating factor, especially as the 3 BOIs are spread over a domain about 50 km wide, so that the modulation we report can be seen on a wide area that covers several grid points at the model resolution of 2.5 km, rather than a very localized small-scale effect. Moreover, if the phenomenon observed was due to one of the intrinsic effects of tide and tidal currents mentioned above, it could be expected to take place either sea ice is present in the area or not. However, the correlation analysis between satellite SWH observations in ice free conditions and tidal currents only explains for a modulation typically equal to what is predicted by the numerical model runs (which, incidentally, is a cross validation of the accuracy of the tidal and wave-current modeling used).

Therefore, it appears that mechanisms independent of the sea ice presence and its damping effect on sea ice consistently fail at reproducing the observations from the BOIs. As a consequence, we deduce from these evidences that the modulation we observe is likely related to the effect of the sea ice on wave propagation, and more specifically to wave in ice attenuation. However, while the model runs with sea ice attenuation successfully reproduce the typical envelope of the observed SWH, the modulation effect is not visible there either. Since the wave model simulations performed with sea ice take into account the sea ice conditions provided from a complete sea ice model that includes time dynamics of the sea ice cover (including changes in the sea ice location, concentration, and thickness), the modulation observed cannot come from simple effects such as changes in the sea ice cover extent, or changes in the shape of large ice tongues leading to changes in the effective wave in ice propagation distance, as these are already reproduced in the simulations. This is further confirmed by a visual inspection of the SAR satellite images of the area over the duration of the modulation event, which confirms that the instruments are evolving relatively deep into the MIZ, and that no drastic changes or surprising features are observed on the ice cover as a whole over the duration of the SWH modulation event. Moreover, the timescale of the modulation event, which shows a period of 12 hours and a total duration of around 3 days, would anyways limit the amount of, for example, ice melting or freezing that can take place. In addition, the WCI model run successfully reproduces the bulk attenuation and the general envelope of the SWH observed at the BOIs, which indicates that the attenuation mechanisms included in the WCI model successfully represent the dominating wave in ice attenuation contribution. Therefore, we conclude that the WCI model is successfully representing a range of physical mechanisms, but that there must exist an additional contribution to wave in ice attenuation, currently not included in the parameterization included in the WCI model, that must cause a periodic increase in wave in ice damping, resulting in the modulation we observe.

At this point, we need to review which mechanism(s) can explain for the periodic increase in the wave in ice damping we observe, evaluate if they are plausible explanations for our observations, and look for the possible signatures or side effects of these mechanisms. A review of the existing literature provides a number of candidate mechanisms for wave in ice attenuation. These are: (i) wave refraction reflection and diffusion due to the hydrodynamic response of the ice floes, (ii) viscoelastic damping in the sea ice, (iii) either laminar or turbulent water-ice friction under the ice due to the wave-induced water velocity, and (iv) floe-floe interactions including hydrodynamic interaction between adjacent floes, collisions, rafting, ridging, and crushing.

If the modulation observed is related to (i: hydrodynamic floe response), this would imply that a major quasi-cyclical change in the floe sizes or shapes takes place, so that the response amplitude operator of the floes (which is a function of their geometry), drastically changes back and forth over a timescale of 12 hours. However, it is not realistic to expect such major back-and-forth change of ice floe geometry over such a short timescale: while it is possible for floes to break relatively fast under the influence of waves, consolidating large floes through re-freezing in an effective enough way so that previously broken floes start behaving as single floe is a slower process.

For (ii: viscoelastic damping) to be the explanation of the modulation, the viscoelastic properties of the sea ice would need to change with a 12 hours period. While it is well established that sea ice mechanical properties can be drastically degraded following, e.g., temperature changes and the impact this has on brine content^{40,106,107}, which can lead to a fast degradation of sea ice Young modulus, this cannot explain for the ice recovering its mechanical properties. Moreover, the atmospheric temperature variations during the wave modulated event are moderate, as visible in Fig. 8. Therefore, the fact that we observe a

periodic change in the effective SWH attenuation, combined with the lack of evidence for large temperature variations in the area during the modulated wave event, makes this explanation unlikely.

Regarding (iii: under ice friction), since the total amount of ice varies relatively little in the area over a 12 hours period, and we would a fortiori not expect that significant melting and re-icing can happen with the 12-hour periodicity we observe, we do not believe that a large change in the water-ice contact area takes place, so that changes to the water-ice area and the implied laminar flow energy dissipation does not appear as a credible explanation. A change in the turbulence level under the ice could modulate the effective eddy viscosity appearing in the equation driving the water-ice stress and the associated energy dissipation, even if the total ice-water area does not change. Such modulation in the amount of turbulence under the ice can come from several sources, in particular, the propagation of the tidal wave through the area of interest, floe-floe collisions, or changes in the relative ice-water velocity. However, if the level of turbulence was strongly modulated in the area due to some phenomenon external to the sea ice, for example tides, more damping would have been observed from satellite altimeter data also in the absence of sea ice. This, in turn, makes us believe that if turbulence level changes participate in causing the observed SWH modulation, these are likely introduced due to some ice mechanisms, such as floe-floe interaction and collision. Change in effective roughness of the sea ice-water interface can also modulate the ice-water stress and dissipation, but for this to play a role here, a periodic 12-hour increase and decrease in the sea ice roughness would be needed. This seems little realistic, as icing and melting mechanisms under the sea ice are not expected to present such strong periodicity, and phenomena such as rafting and ridging would lead to an increase, but no subsequent decrease, in the ice roughness - so that this likely cannot explain for the periodicity we observe. An additional possible mechanism could be that, while the water-ice area of contact and the turbulence level under the ice are not strongly modulated, the degree to which the motion of the ice is horizontally constrained could change with time, following sea ice convergence and divergence. More specifically, when the ice cover, which is constituted of many broken floes of moderate typical size, is "open" following a period of sea ice divergence, ice floes could be able to move to some degree in the horizontal direction, so that the slip velocity between the wave-induced water motion and the ice is reduced. By contrast, when the ice is "closed" following a period of sea ice convergence, the horizontal motion of the floes compressed together and acting as a larger ice sheet may be more strongly constrained, and the slip velocity may be higher. This could lead to different boundary conditions determining the shape of the boundary layer under the ice, and influence the damping induced by under ice boundary layers, as previously discussed in¹⁰⁸. This also could be seen as a secondary effect of floe-floe interaction, since it is the close contact between floes that would prevent the ice to follow the waves. However, the sea ice concentration never reaches 100% in our models in the area of interest, and SAR images confirm that leads and water openings seem to always be observed around the BOIs, and that floes have moderate sizes compared to the typical wavelength. Therefore, the hypothesis that the sea ice may get so tightly packed that ice floe motion get strongly constrained in the horizontal direction at some times compared to others seems unlikely.

The last mechanism (iv: floe-floe interaction) can influence wave in ice damping in several ways. First, collisions per se can dissipate energy, through both sea ice crushing, inelastic collisions, and hydrodynamic pumping effect between the colliding floes^{33,109,110}. Second, collisions, through the hydrodynamic pumping effect and the water jets this creates, inject significant amounts of turbulence under the sea ice¹⁰⁹. This can possibly modulate the amount of turbulent kinetic energy and the effective turbulent eddy viscosity, and create an increase of the damping from the mechanism (iii) previously discussed. The question of the existence of collisions in the MIZ has been slightly polemic in the last few years (while no article explicitly mentions this as being polemic, as far as the authors are aware, this assessment is based on personal communications and discussions received by some of the authors, and reviews received during the publication process of³³). In particular, there are arguments that floes follow the waves in synchronization, so that there are no collisions actually happening between the floes even if all floes move. However, this argument disregards several aspects of waves in ice and the MIZ. First, floes are not identical: as reported by the width of the floe size distribution, different floes have different size and shape, leading to different response amplitude operator characteristics in waves, which would imply the existence of collisions. Second, even though waves in ice at any depth in the MIZ are usually dominated by long-crested swell, there is still stochasticity in the amplitude and wavelength of individual waves. Therefore, even two identical floes next to each other, with the same RAO, can experience collisions if two consecutive waves have different enough height and wavelength. Finally, sea ice cover has many features, such as ridges and keels, that can induce relative motion between floes and create collisions. Similarly, several reviewers have reported during the peer-review of³³ that they had not observed collisions when they were working in the sea ice, and are, therefore, skeptical around the actual occurrence of collisions. However, we believe that this feeling may suffer, at least partially, from a selection bias: to be allowed to deploy, operate, and recover SD-card-containing instruments, sea ice conditions have to be calm enough to allow safe work on sea ice. This is typically not the case for conditions in which sea ice breakup and collisions may happen, therefore, potentially limiting the amount of such events in timeseries records available for analysis. We also note that collisions are the most extreme realization of floe-floe interaction. In particular, it may be possible to have significant floe-floe interaction, including creation of water pumping and water jets between floes, even without a full collision to take place: these effects will take place as soon as a significant change in the short range floe-floe distance takes place, even in the absence of collisions.

Therefore, the results obtained in the Data Analysis section do not seem to be compatible with neither explanations (i) nor (ii), and explanation (iii) can be a contributing factor, but could be present as a bi-product of (iv). As a consequence, (iv), possibly in combination to its effect on modulating (iii), appears following our review of possible mechanisms as the most likely phenomenon that can explain for our in situ observations. However, this conclusion is obtained by a combination of elimination of other possible explanations, and high level discussion of the mechanisms at play. Therefore, more in-situ data will be needed in order to bring a direct positive proof of our circumstanced hypothesis that floe-floe interaction is the explanation for our SWH modulation observation. While this is not attainable for this specific event from 2021, we can suggest additions to the functionality of future OMBs and similar buoys that would allow to provide positive evidence of our conjecture. In particular, it should be easily possible to measure floe-floe collisions, since the signature of such events in the acceleration timeseries recorded by instruments on the sea ice is very characteristic³³. As a consequence, we believe that extending OMB firmware with on-board processing for collision detection to quantify the occurrence of events similar to what is described in³³, and transmitting this information together with the wave spectrum as additional data fields, is a natural next step. This should be easily implementable, since the full time series of the sea ice acceleration is already available on the OMB as it is used for computing the wave spectrum. It should, therefore, be easy to include a high pass filtering analysis of the signal to the firmware, and to use this to count collision events and measure their strength relative to the smoother wave-induced signal. We intend to perform such firmware extensions and include it in our buoys in the near future.

Our conjecture that increased damping could be related to floe-floe interactions being strengthened by sea ice convergence that presses floes together, while reduced damping could be related to floe-floe interaction being reduced by floes being separated under sea ice divergent conditions, seems to be in good agreement with the overall picture provided by Fig. 3 (right). As visible there on the right panel, there is a strong correlation and agreement between sea ice divergence and higher SWH in the MIZ, and sea ice convergence (i.e., negative divergence) and reduced SWH in the MIZ.

In order to quantify our hypothesis, we estimate a proxy for the average attenuation coefficient applicable on waves that have propagated through the MIZ up to the position of the BOI 19648. For this, we can compute a simple estimate using the ERA5 spectrum value E_{out} outside of the sea ice for the peak open water incoming wave frequency $f = 1/12\text{Hz}$, and compare it to the energy content at the same frequency at the location of the buoys as reported by the instruments inside the sea ice, E_{in} . We can then consider the distance of effective sea ice propagation dx as being equal to the MIZ depth having a sea ice concentration of at least 0.5 according to the AMSR2 dataset. After correcting for the propagation time lag δt by matching the peak of the incoming wave energy to the peak of the SWH envelope at the buoys, we can estimate the effective bulk attenuation coefficient α (with unit m^{-1}) as $\alpha = -\ln[E_{in}/E_{out}]/dx$. Note that this estimate is only a coarse proxy to be used to estimate typical orders of magnitude involved, and that it neglects several important effects, e.g. the frequency dependence of the attenuation rate and the associated changes in the mean wave period. Results are presented in Fig. 16. As visible there, the bulk attenuation coefficient α has a typical value of $2 \cdot 10^{-5} \text{m}^{-1}$, respectively $4 \cdot 10^{-5} \text{m}^{-1}$, during high, respectively low, SWH events at the BOI 19648. In other words, the modulation of attenuation leads to a doubling of the effective wave attenuation rate. We note that these values are typically within the expected range: ¹¹¹ reports that typical values for α are within the range $1 \cdot 10^{-5}$ from broken pack ice^{112,113}, to $2 \cdot 10^{-4}$ for solid landfast ice, for the typical frequency range considered. We also observe that our findings are roughly similar to what has been reported by³³: in the corresponding work, collisions and water pumping increasing the turbulent kinetic energy dissipation under the ice floes were found to dissipate around 40% of the total energy input. If we assume that the dominating factor in the change of α is due to the switching on / off of floe-floe interactions, collisions, and enhanced turbulent dissipation, the doubling of α between low and high SWH conditions would similarly correspond to up to 50% of the energy being dissipated by these mechanisms in the cases when α is highest. Naturally, these are only proxy estimates, and the exact numbers would be slightly modulated by a number of factors, including the effect of wave-current interaction which, while it was found too weak to explain for the modulation observations, does contribute to the exact values obtained.

In the present discussion about waves in ice attenuation, we have been focusing on the local processes happening in the neighborhood of the buoys. However, the SWH observed at the location of the buoys is the result of both the local processes happening in the sea ice, but also of the integrated attenuation taking place in the MIZ when the waves travel towards the instruments. Therefore, the complete explanation for the observations may include some non-local effects, and the SWH observed should, in theory, be related to the effect of the sea ice state, including its convergence and divergence rate if these indeed play a role, over the propagating ray of the waves. We have attempted to perform such an analysis. However, the amount of data collected was not sufficient to reach clear conclusions. This points to the need for performing even larger scale deployments involving larger instruments arrays, by continuing to leverage low cost instrumentation such as the OMB. We hope that such deployments will allow, in the future, to measure the progressive attenuation of the SWH through an array covering the entirety of the MIZ, and not just at a few locations deep into the ice.

The present observations are likely related, as we have discussed, to the convergence and divergence of the sea ice induced by the strong tidal currents in the area, and the effect this has on wave in ice attenuation. This makes the present area particularly

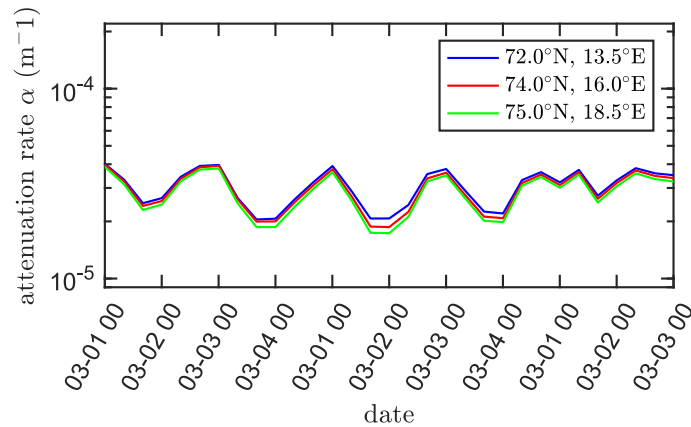


Figure 16. Estimates of the bulk waves in ice attenuation coefficient α for $T = 12$ s period waves across the MIZ for the BOI with ID 19648. The distance between the ice edge and the buoy was estimated from AMSR2 sea ice concentration. Incoming wave energy E_{in} was estimated using the ERA5 reanalysis data. Three different coordinates were used as an ERA5 input, for controlling the insensitivity of the results to changes in the exact choice of the ERA5 data selection location (see figure legend for the exact locations). This confirms that our bulk attenuation coefficient proxy estimate is robust.

interesting to study further, as such tide-driven dynamics should, therefore, be observed reliably in a relatively wide area where strong tidal motions are present. However, the applicability of these observations is likely more general. Indeed, we expect that strong sea ice convergence and divergence effects can also happen without strong driving tidal currents. For example, sudden wind events trigger inertial oscillations which, when they hit the MIZ, will interact with the gradient in sea ice concentration and cause sea ice closing and opening. This implies that the dynamics we observe may play a role in storm conditions anywhere in the MIZ, both in the Arctic and Antarctic, though such events may be less reproducible and less regular than in the present tide-driven conditions. Such modulated waves in ice amplitude events have possibly been observed previously in some satellite observations of the MIZ following the passing of storms (internal correspondence and communication), and should also deserve attention in the future, independently of location and the presence of tidal currents.

5 Conclusion

We report direct in-situ observations from wave buoys in the Arctic MIZ that contain strongly modulated waves-in-ice significant wave height (SWH) records, with a 12-hours SWH modulation period. The modulation ratio observed between consecutive SWH maxima and minima at the buoy deepest into the MIZ goes up to 90%. We show, through a combination of analyses including numerical models, ray tracing analysis, and direct satellite observations in the same area in ice-free conditions, that while tidal modulation takes place in the area, the observed modulation likely cannot be explained by mechanisms such as wave-current interaction, ice drift, or changes of effective wave propagation distance in the sea ice alone. More specifically, our estimations for the strength of wave-current and ice-independent SWH modulation, either these are based on numerical models or satellite data analysis in ice free conditions, conclude that a modulation of typically around 30% can be expected due to the tidal wave-current interaction in the absence of sea ice. Moreover, numerical models including sea ice effect indicate that commonly used wave in ice attenuation parameterizations can explain for the typical bulk attenuation coefficient and the envelope of the SWH observed in the sea ice, but that these cannot explain for the SWH modulation we observe. These results, though they are obtained from numerical models which contain sources of uncertainty and are not an absolute truth, suggest that some additional mechanisms are playing a role in the observations we report.

Therefore, we deduce by elimination that the mechanism(s) explaining for the modulation we observe is likely to be related to the sea ice, and, more specifically, to a modulation of the waves in ice attenuation coefficient. For this, we hypothesize that a time-varying contribution in the wave attenuation is likely playing a key role in the MIZ area we observe, and that such a time-varying component is missing from current state-of-the-art waves in ice attenuation models.

Moreover, we observe that the modulation in the SWH is strongly correlated to the local state of sea ice convergence and divergence. Therefore, we conjecture that the missing variability in the waves in ice attenuation coefficient is possibly arising from the effect of floe-floe interaction, which intensity can be modulated by the strong state of convergence and divergence in the sea ice observed in the area, as visible in both satellite data, buoys trajectories, and model predictions. In particular, we hypothesize that sea ice convergence and divergence, by affecting the closeness between neighboring floes, may switch floe-floe interactions and floe-floe collisions on and off. This is consistent with other recent observations obtained from in-situ

instruments, where the full timeseries of the ice motion were recovered, which analysis indicates that collisions can take place in the MIZ under certain sea ice and wave conditions. This conjecture is also consistent with recent idealized field experiments, in which collisions and the associated forced water motion and turbulence were reported to be able to contribute significantly to the overall wave energy dissipation. Therefore, we observe a convergence of indices that indicate that floe-floe interaction is a likely explanation for the peculiar features present in our in-situ observations.

However, we acknowledge that our results are, at present, speculative to some degree, and should be considered as a circumstanced conjecture. In order to firmly confirm our conjecture, indisputable in-situ evidence of floe-floe interaction dynamics or other modulated waves in ice attenuation mechanism should be collected through a well defined metrics, alongside collocated observations of wave in ice attenuation across the MIZ extent, and the correlation between both phenomena should be examined. While this cannot be achieved in the data from 2021 that we report, we suggest that this information can be obtained in the future by programming waves in ice buoys to report statistics about collisions happening in sea ice, in addition to the information traditionally transmitted. We argue that such additional information should be easy to add to the firmware running on, e.g., the OpenMetBuoys, by applying simple firmware upgrade to buoys to be deployed in the future. Providing direct positive evidence of the existence and importance of such a mechanism would be a major contribution to our understanding of what mechanisms play a role in determining the variability of the observed wave in ice attenuation, and will be an objective for our future measurement campaigns.

We also conclude that the area considered, South-East from Svalbard, is very well suited to investigating complex waves in ice and waves-current interaction phenomena. Indeed, sea ice has historically been very reliably observed in the area during the late Arctic winter, and complex sea ice dynamics in the area are forced by strong tidal currents in a reliable and reproducible way that seems well captured by state-of-the-art models. Therefore, we believe that this area deserves further investigation, and that it is well suited for a range of measurements, from using large numbers of low cost OMB-like buoys in open water and sea ice, to, e.g., long term deployment of bottom mounted acoustic doppler current profiler (ADCP) and pressure sensors, which should be easy to deploy and recover thanks to the limited water depth (typically 35-50m) in the area. We expect possible future findings and improved physical modeling developed based on such measurements to be applicable also in other situations in the MIZ where the sea ice convergence and divergence are due not to tides, but to, e.g., passing storms and inertial oscillations that lead to a sudden series of convergences and extensions of the MIZ.

Acknowledgement

We want to thank the crew of the icebreaker Research Vessel Kronprins Haakon for the invaluable help and support deploying the OMBs buoys during the PC-2 winter process cruise in February 2021. JR gratefully acknowledges funding from the Nansen Legacy Project funded by the Norwegian Research Council to the Norwegian Meteorological Institute (NFR grant AeN, NFR-276730). MM gratefully acknowledges funding from the FOCUS project, funded by the Norwegian Research Council (grant NFR-301450), which also funded the instruments v2021 used in this study.

Appendix A: openly available data and code

All buoy observation data used in the present study are already released as open source data following the publication of⁵¹, see the data available on the Arctic Data Center at <https://adc.met.no/datasets/10.21343/azky-0x44>, or on Github at: https://github.com/jerabaul29/data_release_sea_ice_drift_waves_in_ice_marginal_ice_zone_2022.

Some key codes and scripts used in the present manuscript are available at: https://github.com/jerabaul29/article_data_modulated_attenuation_waves_in_ice_2021_03 (will be released upon acceptance of the manuscript for publication in the peer reviewed literature). Please use the issue tracker there for any further query.

SAR satellite data can be seen on Ocean Virtual Laboratory (OVL) viewer, see for example the view of the corresponding area available at <https://odl.bzh/c840-gF3>.

The satellite wave measurements can be recovered using the wavy python package: <https://github.com/bohlinger/wavy>. The ray tracing analysis can be reproduced using the ocean wave tracing python package: https://github.com/hevgyrt/ocean_wave_tracing.

OVL technical appendix

In order to make Fig. 7 more easily readable, a few custom commands were issued that are not visible directly from the permalink since these are not saved by the OVL tool at the moment. These include (note that these may evolve in the future as the tool further develops):

- The font size is adapted by using the zoom feature of the web browser (Ctrl +/-) and adapt the view area afterwards.

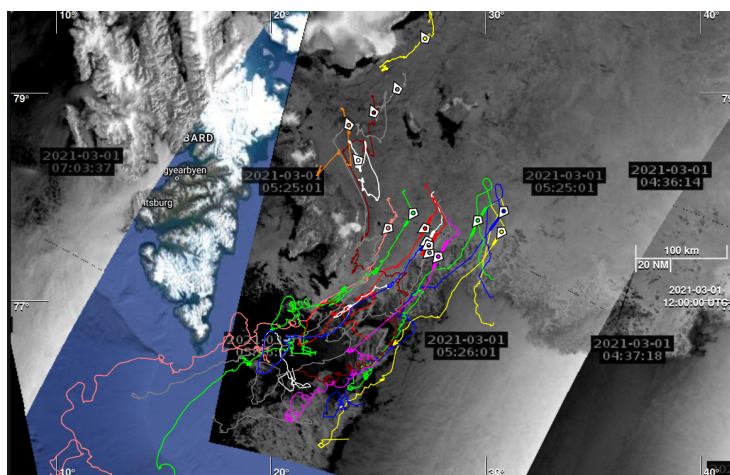


Figure 17. Illustration of the SAR acquisition time reported by the OVL online tool.

- The OMB track weight is tuned through the debug console of the web browser (usually opened with Ctrl-Shift-i), then entering the following command in the prompt:

```
document.querySelectorAll('polyline').forEach(function(polyline){polyline.setAttribute('stroke-width', 2)})
```

- The colormap for the swell first partition is modified using in the debug console of the web browser:

```
var product = ODL.Syntool.productsStore.getProduct('3857_001_027_swell1_vectorfield');
product.dataFields['swh'].max = 3.0;
product.colormaps[0].ticks = ODL.ConfigUtils.makeDeltaTicks(0, 3.0, 0.5);
```

and unselecting then reselecting "Wave 1rst spectral partition from MFWAM model (Météo-France, CMEMS)" in the products list (the one on the left side of the screen) to see the change.

- We hide the user interface and keep only the relevant information on screen by using the shortcut: Shift-f .
- Information about the acquisition time of the SAR images can be obtained in the following way: (i) open a map including SAR data, (ii) enable the pop up from "Display data", (iii) toggle the clock icon close to the SAR layer, labeled "Toggle acquisition datetimes". An example of rendering with this option enabled is shown in Fig. 17.

References

1. NSIDC. National snow and ice data center: Cryosphere and sea ice.
2. Meier, W. N. & Stroeve, J. An updated assessment of the changing arctic sea ice cover. *Oceanography* **35**, 10–19 (2022).
3. Parkinson, C., Claire, L. *et al.* *Earth from above: using color-coded satellite images to examine the global environment* (University science books, 1997).
4. Budikova, D. Role of arctic sea ice in global atmospheric circulation: A review. *Glob. Planet. Chang.* **68**, 149–163 (2009).
5. Overland, J. E., Wood, K. R. & Wang, M. Warm arctic—cold continents: climate impacts of the newly open arctic sea. *Polar Res.* **30**, 15787 (2011).
6. Gao, Y. *et al.* Arctic sea ice and eurasian climate: A review. *Adv. Atmospheric Sci.* **32**, 92–114 (2015).
7. Olsen, J., Hovelsrud, G. K. & Kaltenborn, B. P. Increasing shipping in the arctic and local communities' engagement: A case from longyearbyen on svalbard. *Arct. marine sustainability: arctic maritime businesses resilience marine environment* 305–331 (2020).
8. Shi, Y., Yang, Y., Teng, Y., Sun, M. & Yun, S. Mechanism of sea ice formation based on comprehensive observation data in liaodong bay, china. *J. Oceanol. Limnol.* **37**, 1846–1856 (2019).

9. Müller, M., Knol-Kauffman, M., Jeurig, J. & Palerme, C. Arctic shipping trends during hazardous weather and sea-ice conditions and the polar code's effectiveness. *NPJ Ocean Sustainability* [10.1038/s44183-023-00021-x](https://doi.org/10.1038/s44183-023-00021-x) (2023).
10. Dumont, D. Marginal ice zone dynamics: history, definitions and research perspectives. *Philos. Transactions Royal Soc. A* **380**, 20210253 (2022).
11. Horvat, C. Floes, the marginal ice zone and coupled wave-sea-ice feedbacks. *Philos. Transactions Royal Soc. A* **380**, 20210252 (2022).
12. Thomson, J. Wave propagation in the marginal ice zone: connections and feedback mechanisms within the air–ice–ocean system. *Philos. Transactions Royal Soc. A* **380**, 20210251 (2022).
13. Iwasaki, S. Increase in the wave power caused by decreasing sea ice over the sea of okhotsk in winter. *Sci. Reports* **13**, 2539 (2023).
14. Gao, X. *et al.* Evaluation of sea ice simulation of cas-esm 2.0 in historical experiment. *Atmosphere* **13**, 1056 (2022).
15. Thomson, J. & Rogers, W. E. Swell and sea in the emerging arctic ocean. *Geophys. Res. Lett.* **41**, 3136–3140 (2014).
16. Shao, Z.-D. & Ke, C.-Q. Spring–summer albedo variations of antarctic sea ice from 1982 to 2009. *Environ. Res. Lett.* **10**, 064001 (2015).
17. Squire, V. A., Dugan, J. P., Wadhams, P., Rottier, P. J. & Liu, A. K. Of ocean waves and sea ice. *Annu. Rev. Fluid Mech.* **27**, 115–168 (1995).
18. Zhao, X., Shen, H. H. & Cheng, S. Modeling ocean wave propagation under sea ice covers. *Acta Mech. Sinica* **31**, 1–15 (2015).
19. Zhao, X. & Shen, H. H. Wave propagation in frazil/pancake, pancake, and fragmented ice covers. *Cold Reg. Sci. Technol.* **113**, 71–80 (2015).
20. Sutherland, G. & Rabault, J. Observations of wave dispersion and attenuation in landfast ice. *J. Geophys. Res. Ocean.* **121**, 1984–1997 (2016).
21. Squire, V. A. Ocean wave interactions with sea ice: A reappraisal. *Annu. Rev. Fluid Mech.* **52**, 37–60 (2020).
22. Løken, T. K. *et al.* Wave measurements from ship mounted sensors in the arctic marginal ice zone. *Cold Reg. Sci. Technol.* **182**, 103207 (2021).
23. Sutherland, G., Rabault, J., Christensen, K. H. & Jensen, A. A two layer model for wave dissipation in sea ice. *Appl. Ocean. Res.* **88**, 111–118 (2019).
24. Rabault, J., Sutherland, G., Gundersen, O. & Jensen, A. Measurements of wave damping by a grease ice slick in svalbard using off-the-shelf sensors and open-source electronics. *J. Glaciol.* **63**, 372–381 (2017).
25. Marchenko, A. Wave attenuation in marginal ice zone of arctic pack ice to the north of spitsbergen. In *ISOPE International Ocean and Polar Engineering Conference*, ISOPE–I (ISOPE, 2018).
26. Voermans, J., Babanin, A., Thomson, J., Smith, M. & Shen, H. Wave attenuation by sea ice turbulence. *Geophys. Res. Lett.* **46**, 6796–6803 (2019).
27. Zhang, C. & Zhao, X. Theoretical model for predicting the break-up of ice covers due to wave-ice interaction. *Appl. Ocean. Res.* **112**, 102614 (2021).
28. Zhao, X. & Shen, H. H. Three-layer viscoelastic model with eddy viscosity effect for flexural-gravity wave propagation through ice cover. *Ocean. Model.* **131**, 15–23 (2018).
29. Marchenko, A. *et al.* Laboratory investigations of the bending rheology of floating saline ice and physical mechanisms of wave damping in the hsva hamburg ship model basin ice tank. *Water* **13**, 1080 (2021).
30. Bennetts, L. G., Peter, M. A., Squire, V. & Meylan, M. H. A three-dimensional model of wave attenuation in the marginal ice zone. *J. Geophys. Res. Ocean.* **115** (2010).
31. Zhao, X. & Shen, H. A diffusion approximation for ocean wave scatterings by randomly distributed ice floes. *Ocean. modelling* **107**, 21–27 (2016).
32. Herman, A., Cheng, S. & Shen, H. H. Wave energy attenuation in fields of colliding ice floes–part 1: Discrete-element modelling of dissipation due to ice–water drag. *The Cryosphere* **13**, 2887–2900 (2019).
33. Løken, T. K., Marchenko, A., Ellevold, T. J., Rabault, J. & Jensen, A. Experiments on turbulence from colliding ice floes. *Phys. Fluids* **34** (2022).

34. Voermans, J. J. *et al.* Experimental evidence for a universal threshold characterizing wave-induced sea ice break-up. *The Cryosphere* **14**, 4265–4278 (2020).
35. Ren, H., Zhang, C. & Zhao, X. Numerical simulations on the fracture of a sea ice floe induced by waves. *Appl. Ocean. Res.* **108**, 102527 (2021).
36. Herman, A. Wave-induced stress and breaking of sea ice in a coupled hydrodynamic discrete-element wave–ice model. *The Cryosphere* **11**, 2711–2725 (2017).
37. Sutherland, G. *et al.* Estimating a mean transport velocity in the marginal ice zone using ice-ocean prediction systems. *The Cryosphere* **16**, 2103–2114 (2022).
38. Dai, H.-J., McWilliams, J. C. & Liang, J.-H. Wave-driven mesoscale currents in a marginal ice zone. *Ocean. Model.* **134**, 1–17 (2019).
39. Williams, T. D., Bennetts, L. G., Squire, V. A., Dumont, D. & Bertino, L. Wave–ice interactions in the marginal ice zone. part 1: Theoretical foundations. *Ocean. Model.* **71**, 81–91 (2013).
40. Karulina, M. *et al.* Full-scale flexural strength of sea ice and freshwater ice in spitsbergen fjords and north-west barents sea. *Appl. Ocean. Res.* **90**, 101853 (2019).
41. Voermans, J. J. *et al.* Estimating the elastic modulus of landfast ice from wave observations. *J. Glaciol.* 1–11 (2023).
42. Wang, Y., Holt, B., Erick Rogers, W., Thomson, J. & Shen, H. H. Wind and wave influences on sea ice floe size and leads in the beaufort and hukchi seas during the summer-fall transition 2014. *J. Geophys. Res. Ocean.* **121**, 1502–1525 (2016).
43. Roach, L. A., Bitz, C. M., Horvat, C. & Dean, S. M. Advances in modeling interactions between sea ice and ocean surface waves. *J. Adv. Model. Earth Syst.* **11**, 4167–4181 (2019).
44. Horvat, C., Tziperman, E. & Campin, J.-M. Interaction of sea ice floe size, ocean eddies, and sea ice melting. *Geophys. Res. Lett.* **43**, 8083–8090 (2016).
45. Herman, A., Evers, K.-U. & Reimer, N. Floe-size distributions in laboratory ice broken by waves. *The Cryosphere* **12**, 685–699 (2018).
46. Rabault, J. *et al.* An open source, versatile, affordable waves in ice instrument for scientific measurements in the polar regions. *Cold Reg. Sci. Technol.* **170**, 102955 (2020).
47. Rabault, J. *et al.* Openmetbuoy-v2021: An easy-to-build, affordable, customizable, open-source instrument for oceanographic measurements of drift and waves in sea ice and the open ocean. *Geosciences* **12**, 110 (2022).
48. Kodaira, T. *et al.* An affordable and customizable wave buoy for the study of wave-ice interactions: design concept and results from field deployments. *arXiv preprint arXiv:2308.14361* (2023).
49. Rabault, J. *et al.* Measurements of waves in landfast ice using inertial motion units. *IEEE Transactions on Geosci. Remote. Sens.* **54**, 6399–6408 (2016).
50. Thomson, J. *et al.* Development and testing of microswift expendable wave buoys. *Coast. Eng. J.* 1–13 (2023).
51. Rabault, J. *et al.* A dataset of direct observations of sea ice drift and waves in ice. *Sci. Data* **10**, 251 (2023).
52. Nose, T. *et al.* A comparison of an operational wave-ice model product and drifting wave buoy observation in the central arctic ocean: investigating the effect of sea ice forcing in thin ice cover. *arXiv preprint arXiv:2302.02820* (2023).
53. Nose, T. *et al.* Observation of wave propagation over 1,000 km into antarctica winter pack ice. *arXiv preprint arXiv:2309.13714* (2023).
54. Liu, M., Zhang, X., Chen, P., Wang, J. & Zhong, S. Arctic sea-ice type recognition based on the surface wave investigation and monitoring instrument of the china-french ocean satellite. In *2021 Photonics & Electromagnetics Research Symposium (PIERS)*, 2362–2369 (IEEE, 2021).
55. Collard, F. *et al.* Wind-wave attenuation in arctic sea ice: A discussion of remote sensing capabilities. *J. Geophys. Res. Ocean.* **127**, e2022JC018654 (2022).
56. Shen, X., Zhang, J., Zhang, X., Meng, J. & Ke, C. Sea ice classification using cryosat-2 altimeter data by optimal classifier–feature assembly. *IEEE Geosci. Remote. Sens. Lett.* **14**, 1948–1952 (2017).
57. Horvat, C., Blanchard-Wrigglesworth, E. & Petty, A. Observing waves in sea ice with icesat-2. *Geophys. Res. Lett.* **47**, e2020GL087629 (2020).
58. Nilsen, F. *et al.* Pc-2 winter process cruise (wpc): Cruise report. *The Nansen Leg. Rep. Ser.* (2021).

59. Collins III, C. O., Rogers, W. E., Marchenko, A. & Babanin, A. V. In situ measurements of an energetic wave event in the arctic marginal ice zone. *Geophys. Res. Lett.* **42**, 1863–1870 (2015).
60. Kwok, R., Hunke, E. C., Maslowski, W., Menemenlis, D. & Zhang, J. Variability of sea ice simulations assessed with rgps kinematics. *J. Geophys. Res. Ocean.* **113**, <https://doi.org/10.1029/2008JC004783> (2008). <https://agupubs.onlinelibrary.wiley.com/doi/pdf/10.1029/2008JC004783>.
61. Marchenko, A., Kvamstad, B., Fjørtoft, K., Hoyland, K. & Brazhnikov, D. Characteristics of ice drift in the western barents sea reconstructed by the data of ice trackers deployed on drifting ice of the barents sea in 2008 and 2010. In *Proceedings of the International Conference on Port and Ocean Engineering Under Arctic Conditions*, POAC11-147 (2011).
62. Torres, R. *et al.* Gmes sentinel-1 mission. *Remote. sensing environment* **120**, 9–24 (2012).
63. Marchenko, A. & Kowalik, Z. Tidal wave–elliptic island interaction above the critical latitude. *J. Phys. Oceanogr.* **53**, 683–698 (2023).
64. Collard, F. *et al.* Ocean virtual laboratory: A new way to explore multi-sensor synergy demonstrated over the agulhas region. In *Proceedings of Sentinel-3 for Science Workshop (2-5 June 2015, Venice, Italy)* (ESA, 2015).
65. Dodet, G. *et al.* The Sea State CCI dataset v1: towards a sea state climate data record based on satellite observations. *Earth Syst. Sci. Data* **12**, 1929–1951, [10.5194/essd-12-1929-2020](https://doi.org/10.5194/essd-12-1929-2020) (2020).
66. Bohlinger, P., Breivik, Ø., Economou, T. & Müller, M. A novel approach to computing super observations for probabilistic wave model validation. *Ocean. Model.* **139**, 101404, <https://doi.org/10.1016/j.ocemod.2019.101404> (2019).
67. Spreen, G., Kaleschke, L. & Heygster, G. Sea ice remote sensing using amsr-e 89-ghz channels. *J. Geophys. Res. Ocean.* **113** (2008).
68. Melsheimer, C. & Spreen, G. AMSR2 ASI sea ice concentration data, Antarctic, version 5.4 (NetCDF) (July 2012 - December 2019), [10.1594/PANGAEA.898400](https://doi.org/10.1594/PANGAEA.898400) (2019).
69. Aouf, L. *et al.* On the assimilation of cfosat wave data in the wave model mfwam: Verification phase. In *IGARSS 2019-2019 IEEE international geoscience and remote sensing symposium*, 7959–7961 (IEEE, 2019).
70. Dalphiné, A., Aouf, L., Low-Chune, S., Tressol, M. & Fernandez, E. Product user manual for global ocean wave analysis and forecasting product issue 1.3 (2022).
71. Hersbach, H. *et al.* The era5 global reanalysis. *Q. J. Royal Meteorol. Soc.* **146**, 1999–2049 (2020).
72. Group, T. W. The wam model—a third generation ocean wave prediction model. *J. Phys. Oceanogr.* **18**, 1775–1810 (1988).
73. Günther, H., Hasselmann, S. & Janssen, P. Wamocel Cycle 4 (revised version) (tech. Rep. No. 4) (1992).
74. Yu, J., Rogers, W. E. & Wang, D. W. A new method for parameterization of wave dissipation by sea ice. *Cold Reg. Sci. Technol.* **199**, [10.1016/j.coldregions.2022.103582](https://doi.org/10.1016/j.coldregions.2022.103582) (2022).
75. Breivik, Ø. *et al.* The impact of a reduced high-wind charnock parameter on wave growth with application to the north sea, the norwegian sea, and the arctic ocean. *J. Geophys. Res. Ocean.* **127**, [10.1029/2021JC018196](https://doi.org/10.1029/2021JC018196) (2022).
76. Bengtsson, L. *et al.* The harmonie–arome model configuration in the aladin–hirlam nwp system. *Mon. Weather. Rev.* **145**, 1919–1935 (2017).
77. Batrak, Y., Kourzeneva, E. & Homleid, M. Implementation of a simple thermodynamic sea ice scheme, sice version 1.0-38h1, within the aladin–hirlam numerical weather prediction system version 38h1. *Geosci. Model. Dev.* **11**, 3347–3368 (2018).
78. Röhrs, J. *et al.* Barents-2.5 km v2. 0: an operational data-assimilative coupled ocean and sea ice ensemble prediction model for the barents sea and svalbard. *Geosci. Model. Dev.* **16**, 5401–5426 (2023).
79. Müller, M. *et al.* Characteristics of a convective-scale weather forecasting system for the european arctic. *Mon. Weather. Rev.* **145**, 4771–4787 (2017).
80. Bailey, D. *et al.* Cesm cice5 users guide. *Release CESM CICE5* (2018).
81. Shchepetkin, A. F. & McWilliams, J. C. The regional oceanic modeling system (roms): a split-explicit, free-surface, topography-following-coordinate oceanic model. *Ocean. Modelling* **9**, 347–404 (2005).
82. Sutterley, T. tsutterley/pytmd: v2.0.8, [10.5281/zenodo.8347168](https://doi.org/10.5281/zenodo.8347168) (2023).

83. Sutterley, T. C. *et al.* Antarctic ice shelf thickness change from multimission lidar mapping. *The Cryosphere* **13**, 1801–1817 (2019).
84. Howard, S. L. & Padman, L. Arc2kmtm: Arctic 2 kilometer tide model, <https://doi.org/10.18739/A2PV6B79W> (2021).
85. Marchenko, A., Morozov, E., Kozlov, I. & Frey, D. High-amplitude internal waves southeast of spitsbergen. *Cont. Shelf Res.* **227**, 104523 (2021).
86. Turnbull, I. D. & Marchenko, A. V. Deformation of an ice pack influenced by waves and topographic enhancement of tidal motion near hopen island in the barents sea. *Cold Reg. Sci. Technol.* **194**, 103463 (2022).
87. Kowalik, Z. & Marchenko, A. Tidal motion enhancement on spitsbergen bank, barents sea. *J. Geophys. Res. Ocean.* **128**, e2022JC018539 (2023).
88. Fritzner, S. M., Graverson, R. G., Wang, K. & Christensen, K. H. Comparison between a multi-variate nudging method and the ensemble kalman filter for sea-ice data assimilation. *J. Glaciol.* **64**, 387–396 (2018).
89. Fritzner, S., Graverson, R., Christensen, K. H., Rostosky, P. & Wang, K. Impact of assimilating sea ice concentration, sea ice thickness and snow depth in a coupled ocean–sea ice modelling system. *The Cryosphere* **13**, 491–509 (2019).
90. Duarte, P. *et al.* Implementation and evaluation of open boundary conditions for sea ice in a regional coupled ocean (roms) and sea ice (cice) modeling system. *Geosci. Model. Dev.* **15**, 4373–4392 (2022).
91. Longuet-Higgins, M. S. & Stewart, R. Radiation stresses in water waves; a physical discussion, with applications. *Deep. Res II* **11**, 529–562, [10.1016/0011-7471\(64\)90001-4](https://doi.org/10.1016/0011-7471(64)90001-4) (1964).
92. Masson, D. A Case Study of Wave–Current Interaction in a Strong Tidal Current. *J. Phys. Oceanogr.* **26**, 359–372, [10.1175/1520-0485\(1996\)026<0359:ACSOWI>2.0.CO;2](https://doi.org/10.1175/1520-0485(1996)026<0359:ACSOWI>2.0.CO;2) (1996). *_eprint:* [https://journals.ametsoc.org/jpo/article-pdf/26/3/359/4424891/1520-0485\(1996\)026_0359_acsowi_2_0_co_2.pdf](https://journals.ametsoc.org/jpo/article-pdf/26/3/359/4424891/1520-0485(1996)026_0359_acsowi_2_0_co_2.pdf).
93. Vincent, C. E. The Interaction of Wind-Generated Sea Waves with Tidal Currents. *J. Phys. Oceanogr.* **9**, 748 – 755, [10.1175/1520-0485\(1979\)009<0748:TOWGS>2.0.CO;2](https://doi.org/10.1175/1520-0485(1979)009<0748:TOWGS>2.0.CO;2) (1979). Place: Boston MA, USA Publisher: American Meteorological Society.
94. Saetra, Ø. *et al.* Intense interactions between ocean waves and currents observed in the Lofoten Maelstrom. *J. Phys. Oceanogr.* **-1**, [10.1175/JPO-D-20-0290.1](https://doi.org/10.1175/JPO-D-20-0290.1) (2021). Publisher: American Meteorological Society Section: Journal of Physical Oceanography.
95. Quilfen, Y. & Chapron, B. Ocean Surface Wave-Current Signatures From Satellite Altimeter Measurements. *Geophys. Res. Lett.* **46**, 253–261, <https://doi.org/10.1029/2018GL081029> (2019). *_eprint:* <https://agupubs.onlinelibrary.wiley.com/doi/pdf/10.1029/2018GL081029>.
96. Bôas, A. B. V., Cornuelle, B. D., Mazloff, M. R., Gille, S. T. & Arduin, F. Wave-Current Interactions at Meso- and Submesoscales: Insights from Idealized Numerical Simulations. *J. Phys. Oceanogr.* **50**, 3483 – 3500, [10.1175/JPO-D-20-0151.1](https://doi.org/10.1175/JPO-D-20-0151.1) (2020). Place: Boston MA, USA Publisher: American Meteorological Society.
97. Holthuijsen, L. H. & Tolman, H. L. Effects of the Gulf Stream on ocean waves. *J. Geophys. Res. Ocean.* **96**, 12755–12771, [10.1029/91JC00901](https://doi.org/10.1029/91JC00901) (1991). *_eprint:* <https://onlinelibrary.wiley.com/doi/pdf/10.1029/91JC00901>.
98. Phillips, O. M. *The Dynamics of the Upper Ocean* (Cambridge University Press, Cambridge, 1977), 2 edn.
99. Halsne, T., Christensen, K. H., Hope, G. & Breivik, Ø. Ocean wave tracing v.1: a numerical solver of the wave ray equations for ocean waves on variable currents at arbitrary depths. *Geosci. Model. Dev.* **16**, 6515–6530, [10.5194/gmd-16-6515-2023](https://doi.org/10.5194/gmd-16-6515-2023) (2023). Publisher: Copernicus GmbH.
100. Smit, P. B. & Janssen, T. T. Swell Propagation through Submesoscale Turbulence. *J. Phys. Oceanogr.* **49**, 2615–2630, [10.1175/JPO-D-18-0250.1](https://doi.org/10.1175/JPO-D-18-0250.1) (2019).
101. Kenyon, K. E. Wave refraction in ocean currents. *Deep. Sea Res. Oceanogr. Abstr.* **18**, 1023–1034, [10.1016/0011-7471\(71\)90006-4](https://doi.org/10.1016/0011-7471(71)90006-4) (1971).
102. Smit, P. & Janssen, T. The evolution of inhomogeneous wave statistics through a variable medium. *J. Phys. Oceanogr.* **43**, 1741–1758 (2013).
103. Arduin, F. *et al.* Small-scale open ocean currents have large effects on wind wave heights. *J. Geophys. Res. Ocean.* **122**, 4500–4517 (2017).
104. Halsne, T., Bohlinger, P., Christensen, K. H., Carrasco, A. & Breivik, Ø. Resolving regions known for intense wave–current interaction using spectral wave models: A case study in the energetic flow fields of northern norway. *Ocean. Model.* **176**, 102071 (2022).

105. Gemmrich, J. & Garrett, C. The signature of inertial and tidal currents in offshore wave records. *J. physical oceanography* **42**, 1051–1056 (2012).
106. Ji, S.-y., Wang, A.-l., Su, J. & Yue, Q.-j. Experimental studies on elastic modulus and flexural strength of sea ice in the bohai sea. *J. Cold Reg. Eng.* **25**, 182–195 (2011).
107. Marchenko, A., Morozov, E. & Muzylev, S. Measurements of sea-ice flexural stiffness by pressure characteristics of flexural-gravity waves. *Annals Glaciol.* **54**, 51–60 (2013).
108. Marchenko, A., Wadhams, P., Collins, C., Rabault, J. & Chumakov, M. Wave-ice interaction in the north-west barents sea. *Appl. Ocean. Res.* **90**, 101861 (2019).
109. Rabault, J., Sutherland, G., Jensen, A., Christensen, K. H. & Marchenko, A. Experiments on wave propagation in grease ice: combined wave gauges and particle image velocimetry measurements. *J. Fluid Mech.* **864**, 876–898 (2019).
110. Noyce, M., Verrinder, R. & Vichi, M. Identification of ice floe impacts in an inertial time series and implications for wave measurement in pancake ice. In *IGARSS 2023-2023 IEEE International Geoscience and Remote Sensing Symposium*, 149–152 (IEEE, 2023).
111. Voermans, J. J. *et al.* Wave dispersion and dissipation in landfast ice: comparison of observations against models. *The Cryosphere* **15**, 5557–5575 (2021).
112. Kohout, A. & Williams, M. Waves in-ice observations made during the SIPEX II voyage of the Aurora Australis, 2012, Australian Antarctic Data Centre, doi:10.4225/15/53266bec9607f (2013). Updated 2015.
113. Thomson, J. *et al.* Overview of the arctic sea state and boundary layer physics program. *J. Geophys. Res. Ocean.* **123**, 8674–8687 (2018).